AIChE WILEY InterScience DISCOVER SOMETHING GREAT

REACTORS, KINETICS, AND CATALYSIS

Multicomponent Multicompartment Model for Fischer–Tropsch SCBR

Ion Iliuta and Faïçal Larachi
Dept. of Chemical Engineering, Laval University, Québec, Canada G1K 7P4

Jérôme Anfray
TOTAL, CSTJF, Avenue Larribau, F-64000 Pau, France

Nicolas Dromard
TOTAL, Research Center of Gonfreville, Refining & Process, F-76700 Harfleur, France

Daniel Schweich
LGPC, CNRS, ESCPE, 43 Bd. du 11 Novembre, BP 2077, 69616 Villeurbanne, France

DOI 10.1002/aic.11242
Published online June 27, 2007 in Wiley InterScience (www.interscience.wiley.com).

The Fischer–Tropsch synthesis (FTS) in which a syngas is converted into a wide range of paraffins, olefins, and oxygenates, has found renewed interest in the context of indirect conversion of natural gas. Slurry bubble column reactors (SBCR) rank high among the candidate reactors for FTS. Despite their simple construction, their design are still uncertain because of the fragmented understanding about FTS chemistry, the reactor fluid mechanics, heat and mass transfer, the thermodynamics, and how these phenomena are intermingled in the reactor. A multicomponent/compartment model was developed to account for a detailed hydrodynamics where upon were tied the Fischer–Tropsch and water-gas-shift reactions, the thermodynamics and thermal effects, the variable gas flow-rate because of chemical/physical contraction, and gas and slurry (re)circulation and percompartment back-mixing. A Cobased mechanistic kinetics accounting for olefin re-adsorption was used to describe paraffin and olefin formation and vapor–liquid equilibria were evaluated using a Peng-Robinson/Marano-Holder model. The model was used to analyze the effects of catalyst loading, temperature, gas velocity, water-gas shift, and gas contraction on the performance of SBCRs. The simulated behavior for commercial-scale SBCR was discussed in the light of a sensitivity analysis of the model outputs with regard to the hydrodynamic, the heat and mass transfer parameters. © 2007 American Institute of Chemical Engineers *AIChE J,* 53: 2062–2083, 2007

Keywords: slurry bubble column, Fischer–Tropsch, multicomponent heat and mass transfer, cobalt catalyst, modeling and simulation

Introduction

The discovery of new natural gas reserves, the need to monetize stranded natural gas in remote areas, and the flaring constraints imposed on associated gas, are as many factors leaning in favor of developing new gas transport options for exporting energy from isolated fields to their areas of use. A large technology portfolio is being deployed for energy densification to transport natural gas, such as, gas-to-commodity, gas-to-liquid (GTL), gas-to-solids, and gas-to-wire, besides the more conventional liquefied and compressed natural gas, and pipelines.[1] Prompted by the growing energy needs and

Correspondence concerning this article should be addressed to F. Larachi at faical.larachi@gch.ulaval.ca.

the compelling environmental regulations anticipated to set up in the foreseeable future, the Fischer–Tropsch synthesis (FTS) has been gaining a renewed interest for the conversion of natural gas, predominantly methane, via the GTL route to clean burning motor fuels, lubricants, methanol, plastics manufacture precursors, and so forth.

In commercial FTS, a syngas is converted over Fe or Co catalysts into a complex multicomponent mixture consisting, by and large, of linear hydrocarbons and oxygenates (alcohols, aldehydes, ketones, and esters therefrom). Iron based catalysts are cheap and exhibit a high selectivity to olefins and light hydrocarbons. They are active with respect to water gas shift function and produce large amounts of oxygenates. However, iron catalyst deactivates rapidly because of coke deposition on catalyst surface and oxidative reaction. The supported cobalt catalysts in use industrially yield largely paraffinic products (with some linear α-olefins) at the expense of oxygenates. They are tailored so as to be water-gas-shift negligible and to exhibit high selectivity to higher hydrocarbons owing to a high CO hydrogenation activity, while keeping a low methane make.[2]

Although heat removal is a central issue in the design and safe operation of Fischer–Tropsch reactors, the FTS has been traditionally carried out in fixed-bed reactors. Since recently, slurry bubble column reactors (SBCR) are receiving a growing attention owing to their higher heat removal ability as well as their unfriendliness vis-à-vis hot spots, both vouching for nearly isothermal operation. These strengths are counter balanced by an uncertain scale-up due to inadequate assessment of the back-mixing degree to prevail in the commercial units. As a matter of fact, despite being a simple geometry, the complex interactions between phases in SBCR still defy the elaboration of a faithful modeling framework for trustful reactor design. The quest for a "standard" model capturing the specificities of SBCR and the many couplings arising from the nonisochore, nonisothermal, multidisperse, turbulent, and nontrivial thermodynamics and kinetics is still on the agenda of the industrial and academic community working in the area as probed from the literature surge on the subject.

Numerous investigators in the past have developed conceptual models of SBCR for FTS.[3–14] Given the fairly small particle sizes, the suspension of solids in liquid was often modeled as a single pseudo-homogeneous slurry phase. Viewing the solids as slipless with respect to liquid within the slurry, SBCR were often modeled as two-phase gas-slurry systems. The majority of the literature models assume gradientless concentration of the solids throughout the reactor. Closer to physical reality and following the work of Kato et al.,[3] some models estimated the solids axial concentration profile by means of the sedimentation-dispersion model[4,5] or by mechanistic models, which take into consideration solids (de-) entrainment in the wake of rising bubbles.[15] These models have shown that, in spite of the small size of the solids, the axial profile of the solids concentration in the slurry may not be flat. The shape of the axial profile strongly depends on the slurry properties and the operating conditions. In batch slurry, the catalyst concentration is highest at the bottom of the column and decays exponentially with height. Catalyst axial profiles depend on the direction and magnitude of the slurry inlet velocity in co- and countercurrent.[5]

SBCR operate either in the bubbly or in the churn-turbulent flow regime. In the former regime, the gas phase is adequately modeled assuming uniformly sized bubbles.[16,17] In the latter, bubbles differing in size and shape exist. On the basis of experimental observations and measurements in the churn-turbulent regime,[18,19] bubble size distributions have been approximated as two lumping classes: large and small bubbles. Large bubbles (LB) rise straight up through the column and disengage without recirculation, while small bubbles, because of their lower rise velocity, may experience recirculation within the vessel before they eventually disengage. The double-Dirac bubble size distribution approach has been used in modeling SBCR by de Swart,[6] Maretto and Krishna,[7] van der Laan et al.,[20] and Rados et al.[8] Cross-flow interactions between the small and the LB is either neglected[21] or modeled as infinitely fast to homogenize the species compositions in both bubble classes.[22] As suggested by Rados et al.,[8] both of these approaches are limiting cases while the extent of physical interactions between small and large bubble phases would lie somewhere halfway and would lead to some disparities in the species concentrations.

In a similar fashion, intra-phase back-mixing has been modeled as perfect mixing[7,9,23] or has been ignored by assuming plug flow. Because industrial reactors are likely to be affected by some degree of back-mixing, nonideal flow models accounting for a finite degree of back-mixing, are more appropriate for modeling actual reactor systems. These models fall into two broad categories: axial dispersion models[4,5,8,10,11,22,24] or multicell models.[12,25–27] All of them are simplified descriptions of the flow patterns prevailing in SBCR and seem still inadequate to approximate properly the actual fluid dynamics. While ideal flow models may lead to unsatisfactory design, uncertain axial dispersion coefficients plague the scope of the axial dispersion models.

FTS operates with a change in gas flow rate because of chemical contraction, and in return, physical expansion accompanying the heat released by the reactions, the VLEs for hydrocarbons and water and the mass transfer processes which all meter the species split between gas and liquid phases. Therefore, an appropriate SBCR model should capture this effect and should account for the changes in gas flow rate and consequently, in gas holdup, gas-liquid interfacial area, and bubble size.[8,10,28] This renders the model numerically and computationally demanding, which the existing literature attempted to bypass in various ways. Most of the SBCR models that account for the varying gas flow rate employ a simplified linear relationship tying gas flow rate to conversion[29] and can be applied only in some limited cases.[10] However, a more realistic approach is needed. For that reason, Rados et al.[8,13] developed a 1D dynamic gas-compartmental model for churn-turbulent flow in SBCR in which the change in gas flow rate because of contraction/expansion was accounted for using the overall gas mass balance. This is unlike some of the existing models that linearized the change in gas velocity and gas holdup in space and time, and where gas velocity and holdup are calculated algebraically and updated at each numerical step.[5,11]

The need for FTS SBCR design necessitates improved understanding and quantification of the fluid dynamics and transport

processes[30] coupled with the complex chemistry, the thermodynamics and thermal effects. Notwithstanding, although the advancements accomplished hitherto in the modeling of FTS SBCR are noticeable, none of the available approaches attempted, to the best of our knowledge, to harness into a comprehensive model the following phenomena: (1) catalyst sedimentation/advection/dispersion/lateral exchange (2) coupling to gas buoyancy driven slurry recirculation with the slurry and gas rising in the center and flowing downwards alongside the wall due to gas holdup radial profile,[30] (3) detailed chemical kinetics with the complete products' distribution typical of FTS (i.e., high temperature, pressure, industrial catalyst), (4) scrupulously detailed per-species thermodynamics equilibria, (5) thermal effects, heat transfer, and interfacial temperatures using properly formulated enthalpy balance equations.

Procurement of chemical reaction engineering (CRE) models, embedding the observed physics, for improved SBCR design has a twofold goal.[30] First, the current representation of complex flow pattern in SBCR by the axial dispersion model attempts to lump the description of two many physical phenomena into a single dispersion coefficient which cannot be done in a precise manner.[30] Second, the computational fluid dynamics codes (CFD), based on first principles, have not yet sufficiently matured to be relied on as effective tools for the design of industrial-scale slurry bubble columns.[31,32] Let alone that inclusion of the complex FTS chemistry and the simulation of large-scale units using CFD shift the problem beyond the reach of available computational power. In the interim period, it is essential that our well-rooted CRE models are ameliorated and enriched for better descriptions of mixing, transport, and reaction performances.

This work is offered as an incremental piece of information in this direction and proposes a new multicomponent, core-annulus multi-compartment pseudo 2D two-bubble class model for FTS SBCR harnessing the five aforementioned features. We first summarize the main steps for developing a simplified hydrodynamic platform that serves as a backbone for the CRE model. This latter consists of the hydrodynamic platform whereupon are tied the Fischer–Tropsch and water-gas-shift catalytic reactions, the descriptions of thermodynamics and thermal effects, the variable gas flow rate because of chemical/physical contraction, and the gas and slurry (re)circulation and intra-phase per-compartment back-mixing. In the version proposed in this work, the model still ignores the presence of internals in the SBCR, such as the bundles of cooling coils that are inserted in actual commercial-size reactors and the alterations therefrom that result on the core-annulus structure (e.g., slurry central velocity, gas holdup profile) especially in configurations with relatively high cross-sectional occluded vessel areas. Accounting for the 3D effects introduced by the internals in the model is not an obvious task and it was not our intent to implement it in the present contribution; thus, *sensu stricto*, our model approaches only approximately the aforementioned phenomena of (1) catalyst sedimentation/advection/dispersion/lateral exchange and (2) coupling to gas buoyancy driven slurry recirculation in SBCR with internals. In the second part of the work, we propose to analyze the simulated effects of temperature and superficial gas velocity, and inclusion of water-gas shift (WGS) reaction on reactor performances, and we undertake a sensitivity analysis of the model outputs with regard to the hydrodynamic, the heat and mass transfer parameters. The effects of operating conditions on SBCR performance are also discussed.

Model Formulation

Hydrodynamic platform

A general sketch of a slurry bubble column reactor for FTS is shown in Figure 1. To approximate the SBCR hydrodynamics, a pseudo 2D axisymmetric hydrodynamic core-annulus model was developed to describe the catalyst sedimentation/advection/dispersion/(core-annulus)lateral exchange coupled to gas and slurry (re)circulation. The pseudo 2D feature comes from the fact that the model was split in two blocs to handle the axial dependence of the reactor hydrodynamics because of gas phase contraction, besides a radial dependence imposed by the core-annulus flow structure. In the first bloc, a two-fluid turbulent flow model was used for computing the radial profiles of slurry and gas velocities, of gas holdup, and bubble size. This bloc of the hydrodynamic model adheres closely to the model developed by Gupta et al.[33] for analyzing the residence time distributions of the slurry phase in SBCR. In the second, a coupled axial multi-compartment model accounting for sedimentation, dispersion, advection, and lateral exchanges (liquid–liquid, gas–gas, and solid–solid) was solved for obtaining the longitudinal distributions of the hydrodynamic variables. To our knowledge the philosophy of our proposed sedimentation model is quite different from the conventional sedimentation models used in the literature because it explicates the role of the advective transport of catalyst in the logic of the core-annulus flow structure. To compute the reactor hydrodynamic state, the model requires the overall gas holdup (at entry conditions) as an input and an estimation of the volumetric gas flux transported in the form of small bubbles. Both were estimated using the correlations developed by Krishna.[34]

Slurry and Gas Velocity Profiles. The recirculation model in fully developed flow proposed by Gupta et al.[33] to

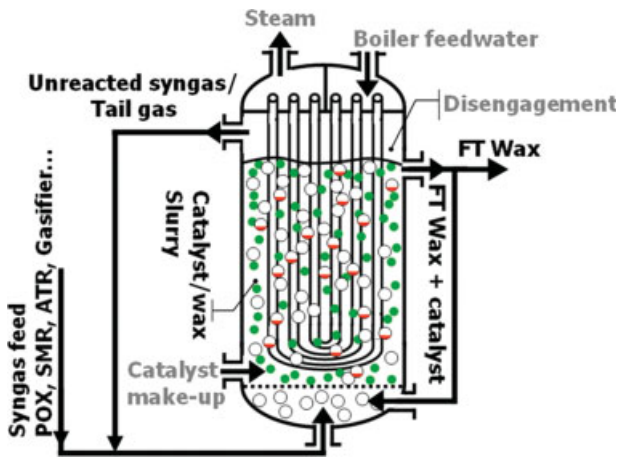

Figure 1. Schematic representation of a slurry bubble column reactor.

[Color figure can be viewed in the online issue, which is available at www.interscience.wiley.com.]

describe the advective transport and turbulent mixing of the gas and slurry phases was used to compute the radial profiles of slurry and gas velocity. The overall momentum balance for the gas/slurry system assuming a fully developed flow is[33]:

$$-g(\varepsilon_g(\xi)\rho_g + (1-\varepsilon_g(\xi))\rho_{ls}) - \frac{dP}{dz} - \frac{1}{R_c\xi}\frac{d}{d\xi}\xi(1-\varepsilon_g(\xi))\tau_{ls}(\xi) = 0 \quad (1)$$

Estimation of the radial slurry velocity profile requires the radial gas holdup profile as input. The gas holdup universal radial profile, structurally similar to that holding for bubble columns, was also shown to be appropriate for SBCR[8]:

$$\varepsilon_g(\xi) = \varepsilon_{g,tot}\frac{m+2}{m+2-2c}(1-c\xi^m) \quad (2)$$

To obtain the radial slurry velocity profile, Eq. 1 was coupled with a turbulence model: a shear turbulence model using a Prandtl–Nikuradse mixing length or the Sato et al.[35] model with bubble-induced and wall shear turbulence. The Prandtl–Nikuradse mixing length turbulence model accounts only for wall shear turbulence, though it was established for single-phase flows, so that turbulence in the slurry is independent of bubbles agitation:

$$\tau_{ls}(\xi) = -\rho_{ls}(\upsilon_{ls} + \upsilon^{turb})\frac{dv_{ls}}{R_c d\xi} \quad (3)$$

$$\upsilon^{turb} = l^2(\xi)\begin{cases} -\dfrac{dv_{ls}}{R_c d\xi} & \xi \le \lambda \\ \dfrac{dv_{ls}}{R_c d\xi} & \xi \ge \lambda \end{cases} \quad (4)$$

$$l(\xi) = (0.14 - 0.08\xi^2 - 0.06\xi^4)R_c \quad (5)$$

In the Sato et al.[35] model, the eddy diffusivity to express the turbulent structure of the slurry phase includes two components: a wall shear induced turbulence[36] (independent of bubbles agitation) and the other for extra turbulence because of the relative motion of gas bubbles. To improve prediction near the wall ($\xi > 0.9$), Sato et al.[35] introduced a dumping factor (Eq. 7):

$$\xi \le 0.9 \quad \tau_{ls}^{turb} = -\rho_{ls}\frac{k}{6}\sqrt{\frac{\tau_w}{\rho_{ls}}}[1-\xi^2][1+2\xi^2]\frac{dv_{ls}}{d\xi}(1-\varepsilon_g) - k_1\rho_{ls}\varepsilon_g\frac{d}{2}v_B\frac{dv_{ls}}{R_c d\xi}(1-\varepsilon_g) \quad (6)$$

$$\xi > 0.9 \quad \tau_{ls}^{turb} = \left\{-\rho_{ls}\frac{k}{6}\sqrt{\frac{\tau_w}{\rho_{ls}}}[1-\xi^2][1+2\xi^2]\frac{dv_{ls}}{d\xi}(1-\varepsilon_g) - k_1\rho_{ls}\varepsilon_g\frac{d}{2}v_B\frac{dv_{ls}}{R_c d\xi}(1-\varepsilon_g)\right\} \times \left\{1 - \exp\left[-\frac{R_c(1-\xi)}{\upsilon_{ls}A^+}\sqrt{\frac{\tau_w}{\rho_{ls}}}\right]\right\}^2 \quad (7)$$

The boundary condition at $\xi = 1$, $v_{ls} = 0$ permits to solve the gas-slurry (re)circulation model and to obtain the slurry radial velocity profile. The solution is attained when the dimensionless radius λ where the maximum negative slurry velocity occurs is found by satisfying the slurry continuity equation and the shear stress balance:

$$\underbrace{\int_0^\lambda (1-\varepsilon_g(\xi))v_{ls}(\xi)\xi d\xi}_{\text{negative/shear-stress}} + \underbrace{\int_\lambda^1 (1-\varepsilon_g(\xi))v_{ls}(\xi)\xi d\xi}_{\text{positive/shear-stress}} = 0 \quad (8)$$

The curvature parameter, m, in Eq. 2 is set so that the centre-line velocity at $\xi = 0$ satisfies a prescribed value. For the simulations of laboratory- and pilot-scale SBCR, this value was formulated using the correlation of Riquarts.[37] For simulating industrial-scale SBCR, the centre-line velocity was formulated as an average value from the Riquarts[37] and Zehner[38] correlations, following comparisons made by van Baten and Krishna.[14] These correlations are given by:

$$v_{ls}|_{\xi=0} = 0.2\sqrt{2R_c g}\left(10^6\frac{U_g^3}{g}\right)^{1/8} \quad (9a)$$

$$v_{ls}|_{\xi=0} = 0.737(2R_c g U_g)^{1/3} \quad (9b)$$

The gas velocity results from solving the gas momentum balance equation after neglecting viscous and turbulent shear stresses in the gas.[33] For bubbles of effective diameter d prevailing at coordinate ξ, the slurry/gas interfacial drag force reduces thus to:

$$\frac{3}{4}\frac{(1-\varepsilon_g(\xi))\rho_{ls}C_D(\xi)}{d(\xi)}(v_{ls}-v_g)|v_{ls}-v_g|\left(\frac{\rho_g}{\rho_g^*}\right)^{0.25} = \left(\frac{dP}{dz} - \rho_g g\right) \quad (10)$$

The slip velocity profile needed for evaluating the local drag coefficient, C_D, derives from knowledge of the slurry and gas velocity profiles:

$$v_{slip}(\xi) = v_g(\xi) - v_{ls}(\xi) \quad (11)$$

Solving Eq. 10 requires knowledge of the pressure gradient and of an effective bubble diameter radial distribution. For simplicity, the bubble effective diameter distribution of Gupta et al.[33] is used:

$$d(\xi) = \delta(1-c\xi^m) \quad (12)$$

The maximum bubble diameter, δ, occurs on the vessel centerline and is chosen so that the gas velocity profile satisfies the gas continuity equation:

$$2\underbrace{\left(\int_0^{\breve{\xi}} \varepsilon_g(\xi)v_g(\xi)\xi d\xi\right)}_{\text{core}} + 2\underbrace{\left(\int_{\breve{\xi}}^1 \varepsilon_g(\xi)v_g(\xi)\xi d\xi\right)}_{\text{annulus}} = U_g \quad (13)$$

Note that $\breve{\xi}$ is the dimensionless radius where inversion occurs, and demarcates the upflowing core from the downflowing annulus. The diameter dependence Eq. 12 is coherent with the picture of the largest bubbles evolving preferentially

in the reactor core, and of diminishing bubble diameters at the approach of column wall. Bubbles in the core are expected to exhibit dependence to surface tension, whereas small bubbles are described by a drag coefficient similar to Schiller-Naumann C_D for Re < 100. The C_D expressions suggested by Tomiyama et al. (see Gupta et al.[33]) are used:

$$C_D(\xi) = \max\left(\frac{24}{\mathrm{Re}(\xi)}(1 + 0.15\mathrm{Re}(\xi)\xi^{0.687}), \frac{8}{3}\frac{Eo(\xi)}{Eo(\xi)+4}\right) \tag{14}$$

To solve for the slurry and gas velocity profiles, the parameters c, m, λ and δ must be known. A number of numerical trials showed that empirical (m, c) correlations, such as those of Wu et al.,[39] did not yield converging solutions in the case of SBCR. Rados[40] also observed that these correlations fail to represent gas holdup and slurry velocity radial profiles for SBCR, especially alongside the wall where they systematically overestimate the local gas holdup. Considering the viscous character of the slurry, it is reasonable to assume that small bubbles will unlikely protrude to the wall ($\xi \approx 1$). It ensues therefore that $c = 1$ is a plausible choice for gas holdup radial distributions in SBCR. For estimating the curvature parameter m, a physical constraint is needed. For this, we have assumed, following a recommendation by Krishna and Sie,[23] that the centerline slurry velocity is estimated reasonably well with the correlation of Riquarts.[37] However, one has to notice that this correlation suffers poor column diameter extrapolability as shown by Forret et al.[41] The parameters δ and λ are chosen so that the gas (respectively, slurry) velocity profile satisfies the gas (respectively, slurry) continuity equation (Eq. 13 respectively, Eq. 8). Note that the pressure gradient can be found by integrating once Eq. 1 and by assigning $\tau_{ls}(\lambda) = 0$.

One additional remark worth mentioning is that the fluid dynamics is likely to be altered in bubble columns because of the presence of bundles of vertical heat-exchange tubes and thus the validity of a core-annulus structure could be questioned. The popularity of core-annulus modeling approaches comes from the fact that these are probably the most evolved 1D models that can handle in a balanced way complexity and richness in hydrodynamic model variables. It is therefore worth to analyze at least qualitatively what happens in the cases of bubble columns with low and high occluded cross-sectional areas due to the internals and the consequences this might have on using core-annulus models. First, we know from experiments that in bubble columns with a low number of internal tubes (i.e., cross-sectional occlusion up to 5%), the radial profiles of liquid axial velocity and gas holdup are barely changed with respect to the internals-free configuration and that the core-annulus flow structure is preserved.[42] This means that for low-occlusion bubble columns, 1D axisymmetric core-annulus model, such as the one developed in this section, would still be fit for describing the advective behavior in both gas and liquid. Therefore, the estimated m and c values, as formulated in Eq. 2, must be an acceptable approximation in bubble columns with a low number of internals. Second, Larachi et al.[32] recently showed through computational fluid dynamics simulations that the qualitative picture of a "core-annulus structure" in bubble columns with internals at high occlusion levels is still preserved provided the internals are distributed uniformly throughout the vessel. However, the value of the central velocity of liquid-and thus the whole velocity radial profile- and consequently the radial profile of gas holdup would be altered with respect to the case of an internals-free bubble column. Such alterations depend on reactor design and construction specificities of the internals (pitch, size, and number density). Extending the applicability of the core-annulus modeling to this case would be possible provided the parameters m and c in Eq. 2 are readjusted in some way to account for the peculiarities of the adopted internals distribution. Preliminary attempts to set equivalences between bubble columns with and without internals at iso cross-sectional areas revealed unfruitful.[32] Thus the issue of analyzing and extending the core-annulus modeling to bubble columns with internals still remains an open question in the literature and deserves in itself dedicated research for improving this type of modeling.

Compartment Model for Recirculation in SBCR. Once the gas and slurry velocity and gas holdup and bubble size radial profiles become known, an axial segmentation is applied to the reactor. The radial location, $\tilde{\xi}$, of slurry velocity inversion is chosen to demarcate ascending from descending regions. Figure 2a sketches a typical radial distribution model showing the slurry and gas interstitial velocity profiles indicating the loci of the dimensionless positions $\tilde{\xi}$ and λ. Figure 2b depicts the proposed flow structure, and the mechanisms and flow variables intervening in the segmentation of the reactor:

- Core small bubbles: volume fraction ε_{SBI} and associated interstitial velocity v_{SBI}.
- Core LB: volume fraction ε_{LB} and associated interstitial velocity v_{LB}.
- Core slurry suspension: volume fraction ε_{LSI} and associated interstitial velocity v_{LSI}.
- Core liquid: volume fraction ε_{LI} and associated interstitial velocity v_{LI}.
- Core solid: mass concentration C_{cI} per unit slurry volume and associated interstitial velocity v_{SI}.
- Annulus small bubbles: volume fraction ε_{SBII} and associated interstitial velocity v_{SBII}.
- Annulus slurry suspension: volume fraction ε_{LSII} and associated interstitial velocity v_{LSII}.
- Annulus liquid: volume fraction ε_{LII} and associated interstitial velocity v_{LII}.
- Annulus solid: mass concentration C_{cII} and associated interstitial velocity v_{SII}.

The above 18 unknowns can be obtained by aggregating the radial profiles obtained earlier for the holdups and velocities (Eqs. 15–20a,b, and 22a,b), and combining them with the slurry compositional relationships (Eqs. 21a,b and 23a,b), the Richardson-Zaki liquid-solid slip velocity correlations (Eqs. 24a,b), the sedimentation/advection/dispersion/lateral exchange equations for transport of the catalyst (Eqs. 25 and 26) and their corresponding boundary conditions (Eqs. 27–30). Some constitutive relationships for the mass transfer coefficient at the core-annulus interface, $\tilde{k}$, and the axial dispersion coefficient in the solid phase, D_s, needed in Eqs. 25 and 26 will be developed later.

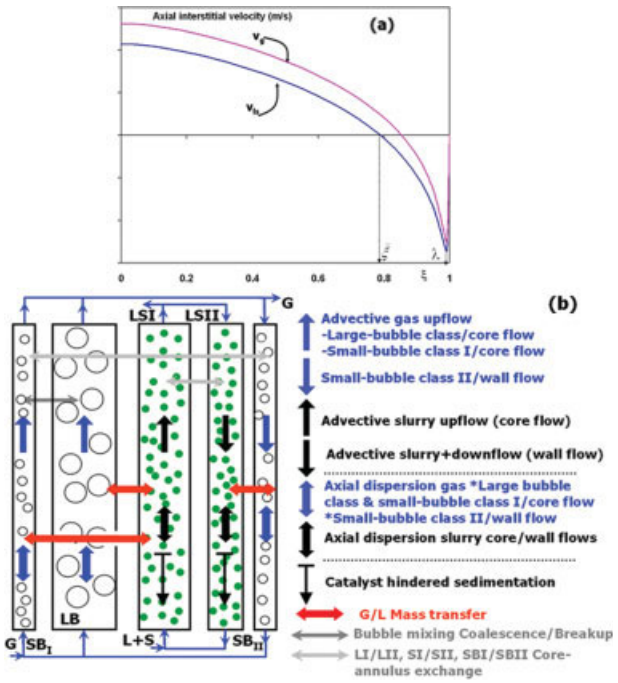

Figure 2. (a) Typical radial profiles of axial velocity of slurry and gas as well as the dimensionless radii for the inversion point and maximum negative slurry velocity (b) Conceptual flow structure and reactor segmentation.

[Color figure can be viewed in the online issue, which is available at www.interscience.wiley.com.]

- Small bubbles holdup in annulus

$$\varepsilon_{\mathrm{SBII}} = 2\int_{\breve{\xi}}^{1} \varepsilon_{\mathrm{g}}(\xi)\xi d\xi \tag{15}$$

- Small bubbles velocity in annulus

$$v_{\mathrm{SBII}} = \frac{2}{\varepsilon_{\mathrm{SBII}}}\int_{\breve{\xi}}^{1} \varepsilon_{\mathrm{g}}(\xi)v_{\mathrm{g}}(\xi)\xi d\xi \tag{16}$$

- Gas holdup in core

$$\varepsilon_{\mathrm{SBI}} + \varepsilon_{\mathrm{LB}} = \varepsilon_{\mathrm{g,tot}} - \varepsilon_{\mathrm{SBII}} \tag{17}$$

- Homogeneous emulsion phase in churn-turbulent flow[23]

$$\varepsilon_{\mathrm{SBI}} = \varepsilon_{\mathrm{SBII}} \tag{18}$$

- Core and small bubbles volumetric fluxes

$$\varepsilon_{\mathrm{SBI}} v_{\mathrm{SBI}} + \varepsilon_{\mathrm{LB}} v_{\mathrm{LB}} = U_{\mathrm{g}} - \varepsilon_{\mathrm{SBII}} v_{\mathrm{SBII}} \tag{19a}$$

$$\varepsilon_{\mathrm{SBI}} v_{\mathrm{SBI}} + \varepsilon_{\mathrm{SBII}} v_{\mathrm{SBII}} = U_{\mathrm{SB}} \tag{19b}$$

- Volume conservation in reactor core and annulus

$$\varepsilon_{\mathrm{SBI}} + \varepsilon_{\mathrm{LB}} + \varepsilon_{\mathrm{LSI}} = \breve{\xi}^2 \tag{20a}$$

$$\varepsilon_{\mathrm{SBII}} + \varepsilon_{\mathrm{LSII}} = 1 - \breve{\xi}^2 \tag{20b}$$

- Core and annulus slurry volume fractions

$$\varepsilon_{\mathrm{LSI}} = \varepsilon_{\mathrm{LI}} + \frac{C_{\mathrm{cI}}}{\rho_{\mathrm{p}}}\varepsilon_{\mathrm{LSI}} \tag{21a}$$

$$\varepsilon_{\mathrm{LSII}} = \varepsilon_{\mathrm{LII}} + \frac{C_{\mathrm{cII}}}{\rho_{\mathrm{p}}}\varepsilon_{\mathrm{LSII}} \tag{21b}$$

- Core and annulus slurry velocities

$$v_{\mathrm{LSI}} = \frac{2}{\varepsilon_{\mathrm{LSI}}}\int_{0}^{\breve{\xi}} (1-\varepsilon_{\mathrm{g}}(\xi))v_{\mathrm{ls}}(\xi)\xi d\xi \tag{22a}$$

$$v_{\mathrm{LSII}} = \frac{2}{\varepsilon_{\mathrm{LSII}}}\int_{\breve{\xi}}^{1} (1-\varepsilon_{\mathrm{g}}(\xi))v_{\mathrm{ls}}(\xi)\xi d\xi \tag{22b}$$

- Core and annulus slurry volumetric fluxes

$$\varepsilon_{\mathrm{LSI}} v_{\mathrm{LSI}} = \varepsilon_{\mathrm{LI}} v_{\mathrm{LI}} + \frac{C_{\mathrm{cl}}}{\rho_{\mathrm{p}}}\varepsilon_{\mathrm{LSI}} v_{\mathrm{SI}} \tag{23a}$$

$$\varepsilon_{\mathrm{LSII}} v_{\mathrm{LSII}} = \varepsilon_{\mathrm{LII}} v_{\mathrm{LII}} + \frac{C_{cII}}{\rho_{\mathrm{p}}}\varepsilon_{\mathrm{LSII}} v_{\mathrm{SII}} \tag{23b}$$

- Core and annulus (Richardson-Zaki) solid slip velocities

$$v_{\mathrm{LI}} - v_{\mathrm{SI}} = v_{\infty}\left(\frac{\varepsilon_{\mathrm{LI}}}{\varepsilon_{\mathrm{LSI}}}\right)^{n-1} \tag{24a}$$

$$v_{\mathrm{LII}} - v_{\mathrm{SII}} = v_{\infty}\left(\frac{\varepsilon_{\mathrm{LII}}}{\varepsilon_{\mathrm{LSII}}}\right)^{n-1} \tag{24b}$$

The axial catalyst concentration profiles were obtained using mass balance equations developed to account for the sedimentation, advection, dispersion of the catalyst as well as the lateral exchange of catalyst between core and annulus:

- Catalyst transport in core by sedimentation/advection/dispersion/lateral exchange

$$\frac{d}{dz}(\varepsilon_{\mathrm{LSI}} C_{\mathrm{cI}} v_{\mathrm{SI}}) = D_{\mathrm{S}}\frac{d}{dz}\left(\varepsilon_{\mathrm{LSI}}\frac{dC_{\mathrm{cI}}}{dz}\right) - \frac{2\breve{\xi}\varepsilon_{\mathrm{LSI}}\varepsilon_{\mathrm{LSII}}}{R_{\mathrm{c}}(\varepsilon_{\mathrm{LSI}}+\varepsilon_{\mathrm{LSII}})}\breve{k}(C_{\mathrm{cI}} - C_{\mathrm{cII}}) \tag{25}$$

- Catalyst transport in annulus by sedimentation/advection/dispersion/lateral exchange

$$\frac{d}{dz}(\varepsilon_{\mathrm{LSII}} C_{\mathrm{cII}} v_{\mathrm{SII}}) = D_{\mathrm{S}}\frac{d}{dz}\left(\varepsilon_{\mathrm{LSII}}\frac{dC_{\mathrm{cII}}}{dz}\right) - \frac{2\breve{\xi}\varepsilon_{\mathrm{LSI}}\varepsilon_{\mathrm{LSII}}}{R_{\mathrm{c}}(\varepsilon_{\mathrm{LSI}}+\varepsilon_{\mathrm{LSII}})}\breve{k}(C_{\mathrm{cII}} - C_{\mathrm{cI}}) \tag{26}$$

- Boundary conditions
  Bottom:

$$-\left(\varepsilon_{\mathrm{LSII}} v_{\mathrm{SII}} C_{\mathrm{cII}}|_{z=0^+} - D_{\mathrm{S}}\varepsilon_{\mathrm{LSII}}\frac{dC_{\mathrm{cII}}}{dz}|_{z=0^+}\right) = \varepsilon_{\mathrm{LSI}} v_{\mathrm{SI}} C_{\mathrm{cI}}|_{z=0^+} - D_{\mathrm{S}}\varepsilon_{\mathrm{LSI}}\frac{dC_{\mathrm{cI}}}{dz}|_{z=0^+} \tag{27}$$

Top:

$$\frac{dC_{cI}}{dz}\Big|_{z=H^-} = 0 \tag{28}$$

$$-\left(\varepsilon_{LSI} v_{SI} C_{cI}\Big|_{z=H^-} - D_S \varepsilon_{LSI} \frac{dC_{cI}}{dz}\Big|_{z=H^-}\right) = \varepsilon_{LSII} v_{SII} C_{cII}\Big|_{z=H^-} - D_S \varepsilon_{LSII} \frac{dC_{cII}}{dz}\Big|_{z=H^-} \tag{29}$$

Overall mass balance:

$$\int_0^H (\varepsilon_{LSI} C_{cI} + \varepsilon_{LSII} C_{cII}) dz = H(\varepsilon_{LSI} + \varepsilon_{LSII}) C_{c0} \tag{30}$$

Mean Bubble Size, Interfacial Area, and Bubble Number Density. The local bubble number density per unit reactor volume is computed from Eqs. 2 and 12:

$$n(\xi) = \frac{\varepsilon_g(\xi)}{\frac{\pi}{6} d^3(\xi)} = \frac{6\varepsilon_{g,tot}(m+2)}{\pi(m+2-2c)\delta^3} \frac{1}{(1-c\xi^m)^2} \tag{31}$$

The gas–liquid interfacial area (per unit local total volume) and the local gas holdup contributed by bubbles with diameter d are, respectively:

$$\pi d^2(\xi) n(\xi) = \frac{6\varepsilon_{g,tot}(m+2)}{(m+2-2c)\delta} \tag{32}$$

$$\frac{\pi}{6} d^3(\xi) n(\xi) = \varepsilon_{g,tot} \frac{m+2}{m+2-2c} (1 - c\xi^m) \tag{33}$$

The Sauter mean bubble diameter, Δ_{SBII}, in the annulus region is obtained as the ratio of the bubbles volume and area contributions for the ξ range $[\breve{\xi} - 1]$:

$$\Delta_{SBII} = \frac{\delta}{6} \frac{\int_{\breve{\xi}}^1 (1 - c\xi^m)}{\int_{\breve{\xi}}^1 \xi d\xi} \tag{34}$$

The following expressions ensue for the mean bubble size and gas–liquid interfacial area in annulus:

$$\frac{d_{SBII}}{\delta} = \frac{\int_{\breve{\xi}}^1 (1 - c\xi^m)\xi d\xi}{\int_{\breve{\xi}}^1 \xi d\xi} \tag{35a}$$

$$a_{SBII} = \frac{6\varepsilon_{SBII}}{d_{SBII}} \tag{35b}$$

The core gas–liquid interfacial area is obtained through integration of Eq. 32 between column centerline and slurry inversion point:

$$a_{SBI} + a_{LB} = 12 \int_0^{\breve{\xi}} \frac{\varepsilon_{g,tot}(m+2)}{(m+2-2c)\delta} \xi d\xi \tag{36}$$

The Sauter core mean bubble diameter is barycentric with respect to the Sauter mean bubble diameters for the small and the LB classes in the core region:

$$\Delta_{SBI/LB} = \frac{a_{SBI}}{a_{SBI} + a_{LB}} \Delta_{SBI} + \frac{a_{LB}}{a_{SBI} + a_{LB}} \Delta_{LB} \tag{37}$$

The Sauter diameter, $\Delta_{SBI/LB}$, is computed from the holdup and area radial profiles over $[0–\breve{\xi}]$ range:

$$\Delta_{SBI/LB} = \frac{\delta}{6} \frac{\int_0^{\breve{\xi}} (1 - c\xi^m)\xi d\xi}{\int_0^{\breve{\xi}} \xi d\xi} \tag{38}$$

Using Eq. 18 and assuming that core and annulus small bubbles are of equal sizes, it ensues that the gas–liquid interfacial area of the small bubbles classes are also equal in core and in annulus:

$$\Delta_{SBI} = \Delta_{SBII} \tag{39a}$$

$$d_{SBI} = d_{SBII} \tag{39b}$$

$$a_{SBI} = a_{SBII} \tag{39c}$$

Equations 35b, 36, and 39c yield the gas–liquid interfacial area, a_{LB}, and Eqs. 34, 37, and 39a retrieve the Sauter mean bubble diameter, Δ_{LB}, for the LB in the core region.

The mean size of the LB in the core is calculated as:

$$d_{LB} = 6\Delta_{LB} \tag{40}$$

The bubble number density per unit reactor volume for each class is derived from knowledge of the per-class bubble diameters and gas hold-ups as:

$$n_{SBI} = \frac{6\varepsilon_{SBI}}{\pi d_{SBI}^3} \tag{41a}$$

$$n_{SBII} = \frac{6\varepsilon_{SBII}}{\pi d_{SBII}^3} \tag{41b}$$

$$n_{LB} = \frac{6\varepsilon_{LB}}{\pi d_{LB}^3} \tag{41c}$$

Core-Annulus Mass Exchange Coefficient and Catalyst Dispersion Coefficient. Using the Kolmogorov isotropic turbulence theory to relate the turbulent kinetic energy, the dissipation of turbulent energy, the eddy size distribution, and the bubble size diameters in the slurry phase, we developed a set of constitutive equations to allow an estimation of the mass transfer of catalyst between core and annulus, $\tilde{k}$, as well as the catalyst dispersion coefficient, D_s, in both core and annulus. These are required for solving Eqs. 25 and 26. Full details unveiling these derivations will be provided in a future work.

Core-annulus mass exchange coefficient:

$$\tilde{k} = 1.4 \frac{5^{5/3} - 1}{20} \sqrt[3]{g U_g d_{LB}} \tag{42}$$

Dispersion coefficient of the solid phase:

$$D_s = \frac{12.6}{620} (5^{5/3} - 1) d_{LB} \sqrt[3]{g U_g d_{LB}} \tag{43}$$

in which d_{LB}, given by Eq. 40, is the diameter of the LB class.

Mass transport/reaction equations

Model Assumptions. The SBCR flow structure was segmented in seven compartments, Figure 2b, each representing:

SBI, LB, SBII, LI, LII, SI, and SII phases. The model accounts for the gas–liquid and liquid–solid mass transfer resistances. Absorption enhancement at the gas–liquid interface because of chemical reaction on the surface of the catalyst was neglected.[43] Given that particle sizes usually encountered in industrial FTS SBCR do not exceed 50 μm and that the FTS intrinsic kinetics is not especially fast, intraparticle temperature and concentration gradients can be ignored. Lateral interactions between SBI and LB are accounted for by means of a bubble–bubble cross-flow mass exchange. The magnitude of SBI↔LB interactions is assumed finite and directly proportional to the flux difference of SBI and LB phases.[8] The model also accounts for the mass transfer between the core and annulus slurries (LSI↔LSII), and between the core and annulus small bubbles (SBI↔SBII). Axial dispersion is assumed to take place in all of the gas and liquid compartments. Furthermore, the catalyst is not uniformly distributed over the entire vessel volume and is computed by the sedimentation/advection/dispersion/lateral exchange model introduced earlier. The model, tailored for the churn-turbulent flow in SBCR, takes into account the contraction of the gas flow rate due to chemical reaction by means of the overall gas mass balance.

The use of two bubble classes is thought to be a pragmatic measure to preserve some physical sense to the model for churn-turbulent flow regimes. Assuming that all the gas is present in the form of single-sized small bubbles-hence, large gas–liquid interfacial area- may lead to an overestimation of conversion if gas–liquid mass transfer is controlling. Moreover, if one accounts for two-bubble classes but ignores bubble–bubble interactions, e.g., SBI↔LB or SBI↔SBII, the calculated conversion could be lower than what should be expected. For example, the larger bubbles gas holdup contributing to LB would bypass the reactor without replenishing the more active small bubble class SBI via SBI↔LB or SBII via SBI↔SBII since the interfacial areas are such that $a_{LB} < a_{SBI}, a_{SBII}$.

Regarding the mass transfer fluxes of components across the gas–liquid interface, we resorted for simplification to the simpler approach in which the interfacial component-wise fluxes are cast as the product of the bulk molar concentration difference times an overall volumetric mass transfer coefficient K_j^0-computed for each individual component using literature correlations we will discuss later on. Two limitations of our approach rest on potential inconsistencies that could arise due to (i) the neglect of the contribution of the barycentric mass transfer due to the total (convective) molar flux traversing the interface, (ii) the nonfulfillment of the null equality from the summation of all the interfacial *diffusion* fluxes.[44] A more rigorous formulation would have required the use of Stefan-Maxwell multicomponent mass transfer rates,[44] which would have resulted in dealing with model complexity beyond the scope of the proposed work considering the very large number of components in play in the case of FTS. Therefore, we leave this part of the problem as a challenge for future studies and will content ourselves with a cruder estimation method.

Species Balance Equations. Under the foregoing assumptions, the steady-state species balance equations for the gas (SBI, LB, and SBII), liquid (LI and LII) and solid compartments (SI and SII) and the corresponding boundary conditions are formulated later. To avoid burdening the text with the meaning of all the variables intervening in these equations, the reader can consult the detailed nomenclature at the end.

j-species in SBI

$$\frac{d}{dz}(\varepsilon_{SBI} v_{SBI} C_{j,SBI}) = \frac{d}{dz}\left(\varepsilon_{SBI} D_s \frac{dc_{j,SBI}}{dz}\right) - {}^{LI}_{SBI}K_j^0 a_{SBI}\left[c_{j,SBI} - {}^{LI}_{SBI}He_j c_{j,LI}\right] - \tilde{k}\varepsilon_{SBI}\frac{\tilde{\xi}}{R_c}(c_{j,SBI} - c_{j,SBII}) - (v_{LB}\varepsilon_{LB} - v_{SBI}\varepsilon_{SBI})\frac{k_{SBI-LB}}{H}(c_{j,SBI} - c_{j,LB}) \quad (44)$$

j-species in LB

$$\frac{d}{dz}(\varepsilon_{LB} v_{LB} c_{j,LB}) = \frac{d}{dz}\left(\varepsilon_{LB} D_{LB} \frac{dc_{j,LB}}{dz}\right) - {}^{LI}_{LB}K_j^0 a_{LB}[c_{j,LB} - {}^{LI}_{LB}He_j c_{j,LI}] - (v_{LB}\varepsilon_{LB} - v_{SBI}\varepsilon_{SBI})\frac{k_{SBI-LB}}{H}(c_{j,LB} - c_{j,SBI}) \quad (45)$$

j-species in SBII

$$\frac{d}{dz}(\varepsilon_{SB_{II}} v_{SB_{II}} c_{j,SB_{II}}) = \frac{d}{dz}\left(\varepsilon_{SBII} D_s \frac{dc_{j,SBII}}{dz}\right) - {}^{LII}_{SBII}K_j^0 a_{SBII}[c_{j,SBII} - {}^{LII}_{SBII}He_j c_{j,LII}] - \tilde{k}\varepsilon_{SBI}\frac{\tilde{\xi}}{R_c}(c_{j,SBII} - c_{j,SBII}) \quad (46)$$

j-species in LI

$$\frac{d}{dz}(\varepsilon_{LI} v_{LI} c_{j,LI}) = \frac{d}{dz}\left(\varepsilon_{LI} D_s \frac{dc_{j,LI}}{dz}\right) + {}^{LI}_{SBI}K_j^0 a_{SBI}[c_{j,SBI} - {}^{LI}_{SBI}He_j c_{j,LI}] - k_{j,LS} a_{LS}(c_{j,LI} - c^s_{j,LI}) + {}^{LI}_{LB}K_j^0 a_{LB}[c_{j,LB} - {}^{LI}_{LB}He_j c_{j,LI}] - \frac{\tilde{k}\varepsilon_{LI}\varepsilon_{LII}}{\varepsilon_{LI} + \varepsilon_{LII}}\frac{2\bar{\xi}}{R_c}(c_{j,LI} - c_{j,LII}) \quad (47)$$

j-species in SI

$$-k_{H_2,LS} a_{LSI}(c_{H_2,LI} - c^s_{H_2,LI}) = -\varepsilon_{LI} C_{cI} R^{SI}_{H_2} + \varepsilon_{LI} C_{cI} R^{SI}_{WGS} \quad \text{for } H_2 \quad (48)$$

$$-k_{CO,LS} a_{LSI}(c_{CO,LI} - c^s_{CO,LI}) = -\varepsilon_{LI} C_{cI} R^{SI}_{CO} - \varepsilon_{LI} C_{cI} R^{SI}_{WGS} \quad \text{for CO} \quad (49)$$

$$-k_{H_2O,LS} a_{LSI}(c_{H_2O,LI} - c^s_{H_2O,LI}) = \varepsilon_{LI} C_{cI} R^{SI}_{H_2O} - \varepsilon_{LI} C_{cI} R^{SI}_{WGS} \quad \text{for } H_2O \quad (50)$$

$$-k_{CO_2,LS} a_{LSI}(c_{CO_2,LI} - c^s_{CO_2,LI}) = \varepsilon_{LI} C_{cI} R^{SI}_{WGS} \quad \text{for } CO_2 \quad (51)$$

$$-k_{j,\mathrm{LS}}a_{\mathrm{LSI}}(c_{j,\mathrm{LI}}-c^{s}_{j,\mathrm{LI}})=\varepsilon_{\mathrm{LSI}}C_{\mathrm{cI}}R^{SI}_{j}$$
$$J=\text{hydrocarbon species} \quad (52)$$

j-species in LII

$$\frac{d}{dz}(\varepsilon_{\mathrm{LII}}v_{\mathrm{LII}}c_{j,\mathrm{LII}})=\frac{d}{dz}\left(\varepsilon_{\mathrm{LII}}D_{s}\frac{dc_{j,\mathrm{LII}}}{dz}\right)+{}^{\mathrm{LII}}_{\mathrm{SBII}}K^{0}_{j}a_{\mathrm{SBII}}[c_{j,\mathrm{SBII}}-{}^{\mathrm{LII}}_{\mathrm{SBII}}He_{j},c_{j,\mathrm{LII}}]-\frac{\tilde{k}\varepsilon_{\mathrm{LI}}\varepsilon_{\mathrm{LII}}}{\varepsilon_{\mathrm{LI}}+\varepsilon_{\mathrm{LII}}}\frac{2\bar{\xi}}{R_{c}}(c_{j,\mathrm{LII}}-c_{j,\mathrm{LI}})-k_{j,\mathrm{LS}}a_{\mathrm{LS}}(c_{j,\mathrm{LII}}-c^{s}_{j,\mathrm{LII}}) \quad (53)$$

j-species in SII

$$-k_{\mathrm{H_2,LS}}a_{\mathrm{LSII}}(c_{\mathrm{H_2,LII}}-c^{s}_{\mathrm{H_2,LII}})=-\varepsilon_{\mathrm{LII}}C_{\mathrm{cII}}R^{\mathrm{SII}}_{\mathrm{H_2}}+\varepsilon_{\mathrm{LII}}C_{\mathrm{cII}}R^{\mathrm{SII}}_{\mathrm{WGS}}\quad\text{for }H_2 \quad (54)$$

$$-k_{\mathrm{CO,LS}}a_{\mathrm{LSII}}(c_{\mathrm{co,LII}}-c^{s}_{\mathrm{CO,LII}})=-\varepsilon_{\mathrm{LII}}C_{\mathrm{cII}}R^{\mathrm{SII}}_{\mathrm{CO}}-\varepsilon_{\mathrm{LII}}C_{\mathrm{cII}}R^{\mathrm{SII}}_{\mathrm{WGS}}\quad\text{for CO} \quad (55)$$

$$-k_{\mathrm{H_2O,LS}}a_{\mathrm{LSII}}(c_{\mathrm{H_2O,LII}}-c^{s}_{\mathrm{H_2O,LII}})=\varepsilon_{\mathrm{LII}}C_{\mathrm{cII}}R^{\mathrm{SII}}_{\mathrm{H_2O}}-\varepsilon_{\mathrm{LII}}C_{\mathrm{cII}}R^{\mathrm{SII}}_{\mathrm{WGS}}\quad\text{for }H_2O \quad (56)$$

$$-k_{\mathrm{CO_2,LS}}a_{\mathrm{LSII}}(c_{\mathrm{CO_2,LII}}-c^{s}_{\mathrm{CO_2,LII}})=\varepsilon_{\mathrm{LII}}C_{\mathrm{cII}}R^{\mathrm{SII}}_{\mathrm{WGS}}\quad\text{for }H_2O \quad (57)$$

$$-k_{j,\mathrm{LS}}a_{\mathrm{LSII}}(c_{j,\mathrm{LII}}-c^{s}_{j,\mathrm{LII}})=\varepsilon_{\mathrm{LSII}}C_{\mathrm{cII}}R^{\mathrm{SII}}_{j}$$
$$j=\text{hydrocarbon species} \quad (58)$$

Gas phase (SBI, LB, SBII) boundary conditions

$$U_{\mathrm{SB}}c^{\mathrm{in}}_{j}-\left(v_{\mathrm{SBII}}\varepsilon_{\mathrm{SBII}}c_{j,\mathrm{SBII}}\big|_{z=0^{+}}-D_{s}\varepsilon_{\mathrm{SBII}}\frac{dc_{j,\mathrm{SBII}}}{dz}\Big|_{z=0^{+}}\right)=v_{\mathrm{SBI}}\varepsilon_{\mathrm{SBI}}c_{j,\mathrm{SBI}}\big|_{z=0^{+}}-D_{s}\varepsilon_{\mathrm{SBI}}\frac{dc_{j,\mathrm{SBI}}}{dz}\Big|_{z=0^{+}} \quad (59)$$

$$\frac{dc_{j,\mathrm{SBI}}}{dz}\Big|_{z=\mathrm{H}^{-}}=0 \quad (60)$$

$$U_{\mathrm{LB}}c^{\mathrm{in}}_{j}=v_{\mathrm{LB}}\varepsilon_{\mathrm{LB}}c_{j,\mathrm{LB}}\Big|_{z=0^{+}}-D_{\mathrm{LB}}\varepsilon_{\mathrm{LB}}\frac{dc_{j,\mathrm{LB}}}{dz}\Big|_{z=0^{+}} \quad (61a)$$

$$\frac{dc_{j,\mathrm{LB}}}{dz}\Big|_{z=\mathrm{H}^{-}}=0 \quad (61b)$$

$$U_{\mathrm{SB}}C_{j,\mathrm{SBI}}\big|_{z=\mathrm{H}^{-}}-\left(v_{\mathrm{SBI}}\varepsilon_{\mathrm{SBI}}c_{j,\mathrm{SBI}}\big|_{z=\mathrm{H}^{-}}-D_{s}\varepsilon_{\mathrm{SBI}}\frac{dc_{j,\mathrm{SBI}}}{dz}\Big|_{z=\mathrm{H}^{-}}\right)=v_{\mathrm{SBII}}\varepsilon_{\mathrm{SBII}}c_{j,\mathrm{SBII}}\big|_{z=\mathrm{H}^{-}}-D_{s}\varepsilon_{\mathrm{SBII}}\frac{dc_{j,\mathrm{SBII}}}{dz}\Big|_{z=\mathrm{H}^{-}} \quad (62a)$$

$$\frac{dc_{j,\mathrm{SBII}}}{dz}\Big|_{z=0^{+}}=0 \quad (62b)$$

Liquid phase (LI, LII) boundary conditions

$$-\left(v_{\mathrm{LII}}\varepsilon_{\mathrm{LII}}c_{j,\mathrm{LII}}\big|_{z=0^{+}}-D_{s}\varepsilon_{\mathrm{LII}}\frac{dc_{j,\mathrm{LII}}}{dz}\Big|_{z=0^{+}}\right)=v_{\mathrm{LI}}\varepsilon_{\mathrm{LI}}c_{j,\mathrm{LI}}\big|_{z=0^{+}}-D_{s}\varepsilon_{\mathrm{LI}}\frac{dc_{j,\mathrm{LI}}}{dz}\Big|_{z=0^{+}} \quad (63a)$$

$$\frac{dc_{j,\mathrm{LI}}}{dz}\Big|_{z=\mathrm{H}^{-}}=0 \quad (63b)$$

$$-\left[\left(v_{\mathrm{LI}}\varepsilon_{\mathrm{LI}}c_{j,\mathrm{LI}}\big|_{z=\mathrm{H}^{-}}-D_{s}\varepsilon_{\mathrm{LI}}\frac{dc_{j,\mathrm{LI}}}{dz}\Big|_{z=\mathrm{H}^{-}}\right)-Lc_{j,\mathrm{LI}}\big|_{z=\mathrm{H}^{-}}\right]-v_{\mathrm{LII}}\varepsilon_{\mathrm{LII}}c_{j,\mathrm{LII}}\big|_{z=\mathrm{H}^{-}}-D_{s}\varepsilon_{\mathrm{LII}}\frac{dc_{j,\mathrm{LII}}}{dz}\Big|_{z=\mathrm{H}^{-}} \quad (64a)$$

$$\frac{dc_{j,\mathrm{LII}}}{dz}\Big|_{z=0^{+}}=0 \quad (64b)$$

The boundary conditions for the liquid phase (LII) were obtained considering that the liquid stream is withdrawn continuously to maintain a constant liquid level in the reactor.[45] The exit liquid stream is assumed to have achieved vapor–liquid equilibrium with a gas composition corresponding to that of the exiting gas phase. It was calculated using the method recommended by Caldwell and van Vuuren.[45]

The species mass balance equations for SI and SII phases are given by Eqs. 48–52 and 54–58, respectively. In these equations, the subscript designates the jth species reaction rate calculated by using the species concentrations at the particle external surface.

FTS operates with a change in gas flow rate because of chemical contraction, and also physical expansion accompanying the heat released by the reactions, the VLEs for hydrocarbons and water and the mass transfer processes which all affect the species partition between gas and liquid. In the present work, the change in gas flow rate is updated at each elevation along the reactor from an overall gas mass balance equation that includes SBI, SBII, and LB compartments:

$$\frac{d}{dz}(U_{g}C_{G})=-\sum_{j=1}^{n}{}^{\mathrm{LI}}_{\mathrm{SB_I}}K^{0}_{j}a_{\mathrm{SB_I}}[c_{j,\mathrm{SB_I}}-{}^{\mathrm{LI}}_{\mathrm{SB_I}}He_{j}c_{j,\mathrm{L_I}}]-\sum_{j=1}^{n}{}^{\mathrm{LI}}_{\mathrm{LB}}K^{0}_{j}a_{\mathrm{LB}}[c_{j,\mathrm{LB}}-{}^{\mathrm{LI}}_{\mathrm{LB}}He_{j}c_{j,\mathrm{L_I}}]-\sum_{j=1}^{n}{}^{\mathrm{LII}}_{\mathrm{SB_{II}}}K^{0}_{j}a_{\mathrm{SB_{II}}}[c_{j,\mathrm{SB_{II}}}-{}^{\mathrm{LII}}_{\mathrm{SB_{II}}}He_{j}c_{j,\mathrm{L_{II}}}] \quad (65)$$

The link with the radial momentum balance equations in the hydrodynamic section regarding the estimation of the radial slurry and gas velocity profiles is done through Eq. 13 above that represents the local continuity equation for a given elevation z in the SBCR for the gas phase.

Note that magnitude of the chemically-produced liquid product stream was found to be on average 500 times lesser

than the bubble-induced liquid circulation rate in the SBCR. This supposes that the liquid flow rate change because of chemical production over a distance dz from height z to $z + dz$ in the SBCR remain so small that the slurry continuity equation (Eq. 8) can still be relied on to compute, in conjunction with the updated gas velocity radial profile, the slurry radial velocity profile at height z.

Lumping–Delumping Equations. The FTS reactor model uses pseudocomponents lumped according to the number of carbon atoms to decrease the computational effort of model simulations. A lumping–delumping approach similar to that proposed by Ahon et al.[9] was followed. Each lump contains $K + 1$ hydrocarbon species. In this work, lumping is initiated at rank C_λ ($\lambda' \geq 5$). The number of carbons in the longest hydrocarbon chain (N), K and λ' are chosen so that $N - (\lambda' - 1)$ is a multiple of $K + 1$ to yield an integer number of lumps $\frac{N-(\lambda'-1)}{K+1}$. The main expressions for the lumping–delumping process are summarized in Appendix A.

Enthalpy balance equations

The change in temperature in every gas and liquid compartment was calculated from the gas- and liquid-phase enthalpy balance equations in which all gas–liquid interfacial heat-transfer resistances and the thermal effects associated with phase change were taken into account. The gas–liquid interfacial temperatures at SBI-LI, LB-LI, and SBII-LII were estimated using the continuity of the energy flux across interfaces.[44] The enthalpy terms H_{SI} (Eq. 72) and H_{SII} (Eq. 74) in the liquid enthalpy conservation equations take into account both the FTS and the WGS reaction heats, ΔH_{FT} and ΔH_{WGS}. According to Eqs. 73 and 75, they have been viewed as volumetric heat source terms issued from the catalyst provided we assume that the catalyst does not exchange heat fluxes other than with the liquid phase. All the liquid–solid interfacial heat transfer resistances are neglected. The solid phase is assumed in thermal equilibrium with the liquid phase because of the high intensity mixing in the column. Finally, we have chosen to account for the heat removed internally at the slurry-cooling tube interfaces because of FTS and WGS reaction exothermicity in a approximate manner as shown by the fourth term (first line) in enthalpy balance equations Eqs. 72 and 74. As a matter of fact, accounting for the heat removed at regular radial interfaces would have imposed the use of 2D r-z models which would have been in opposition with the 1D compartmental philosophy our model is based upon.

For model comprehensiveness, we considered also dissipation of mechanical energies related to the advection in the small and LB and the liquid, the turbulent kinetic energy induced by the LB and the liquid, and the thermal effects due to the gas turbulence inside the LB, the energy dissipation because of axial dispersion in the gas and liquid phases. Sensitivity analysis of these terms concluded they are negligible with respect to the other enthalpy and heat flux terms. Thus the version of the enthalpy balance equations ultimately retained does not include these (mechanical dissipation) terms. The readers can consult the nomenclature for the meaning of the variables in the following equations.

Enthalpy balance in SBI (core flow)

$$\sum_j {}^{\mathrm{LI}}_{\mathrm{SBI}}K_j^0 a_{\mathrm{SBI}}[c_{j,\mathrm{SBI}} - {}^{\mathrm{LI}}_{\mathrm{SBI}}He_j c_{j,\mathrm{LI}}]\overline{H}_j^{\mathrm{SBI}} + \dot{h}_{\mathrm{SBI}}(T^*_{\mathrm{SBI}} - T_{\mathrm{SBI}})a_{\mathrm{SBI}} - \varepsilon_{\mathrm{SBI}} v_{\mathrm{SBI}}\left(\sum_j c_{j,\mathrm{SBI}}\frac{d\overline{H}_j^{\mathrm{SBI}}}{dz}\right) + \frac{d}{dz}\left(\tilde{\lambda}_{\mathrm{SBI}}\varepsilon_{\mathrm{SBI}}\frac{dT_{\mathrm{SBI}}}{dz}\right) = 0 \quad (66)$$

Enthalpy balance at SBI-LI interface (core flow)

$$\sum_j {}^{\mathrm{LI}}_{\mathrm{SBI}}K_j^0 a_{\mathrm{SBI}}[c_{j,\mathrm{SBI}} - {}^{\mathrm{LI}}_{\mathrm{SBI}}He_j c_{j,\ \mathrm{LI}}]\overline{H}_j^{\mathrm{SBI}} - \sum_j {}^{\mathrm{LI}}_{\mathrm{SBI}}K_j^0 a_{\mathrm{SBI}}[c_{j,\mathrm{SBI}} - {}^{\mathrm{LI}}_{\mathrm{SBI}}He_j c_{j,\mathrm{LI}}]\overline{H}_j^{\ \mathrm{LI}} = \dot{h}_{\mathrm{LI}}(T^*_{\mathrm{SBI}} - T_{\ \mathrm{LI}})a_{\mathrm{SBI}} - \dot{h}_{\mathrm{SBI}}(T_{\mathrm{SBI}} - T^*_{\mathrm{SBI}})a_{\mathrm{SBI}} \quad (67)$$

Enthalpy balance in LB (core flow)

$$\sum_j {}^{\mathrm{LI}}_{\mathrm{LB}}K_j^0 a_{\mathrm{LB}}[c_{j,\mathrm{LB}} - {}^{\mathrm{LI}}_{\mathrm{LB}}He_j c_{j,\mathrm{LI}}]\overline{H}_j^{\mathrm{LB}} + \dot{h}_{\mathrm{LB}}(T^*_{\mathrm{LB}} - T_{\mathrm{LB}})a_{\mathrm{LB}} - \varepsilon_{\mathrm{LB}} v_{\mathrm{LB}}\left(\sum_j c_{j,\mathrm{LB}}\frac{d\overline{H}_j^{\mathrm{LB}}}{dz}\right) + \frac{d}{dz}\left(\tilde{\lambda}_{\mathrm{LB}}\varepsilon_{\mathrm{LB}}\frac{dT_{\mathrm{LB}}}{dz}\right) = 0 \quad (68)$$

Enthalpy balance at LB-LI interface (core flow)

$$\sum_j {}^{\mathrm{LI}}_{\mathrm{LB}}K_j^0 a_{\mathrm{LB}}[c_{j,\mathrm{LB}} - {}^{\mathrm{LI}}_{\mathrm{LB}}He_j c_{j,\mathrm{LI}}]\overline{H}_j^{\mathrm{LB}} - \sum_j {}^{\mathrm{LI}}_{\mathrm{LB}}K_j^0 a_{\mathrm{LB}}[c_{j,\mathrm{LB}} - {}^{\mathrm{LI}}_{\mathrm{LB}}He_j c_{j,\mathrm{LI}}]\overline{H}_j^{\mathrm{LI}} = \dot{h}_{\mathrm{LI}}(T^*_{\mathrm{LB}} - T_{\mathrm{LI}})a_{\mathrm{LB}} - \dot{h}_{\mathrm{LB}}(T_{\mathrm{LB}} - T^*_{\mathrm{LB}})a_{\mathrm{LB}} \quad (69)$$

Enthalpy balance in SBII (annulus flow)

$$\sum_j {}^{\mathrm{LII}}_{\mathrm{SBII}}K_j^0 a_{\mathrm{SBII}}[c_{j,\mathrm{SBII}} - {}^{\mathrm{LII}}_{\mathrm{SBII}}He_j c_{j,\mathrm{LII}}]\overline{H}_j^{\mathrm{SBII}} + \dot{h}_{\mathrm{SBII}}(T^*_{\mathrm{SBII}} - T_{\mathrm{SBII}})a_{\mathrm{SBII}} - \varepsilon_{\mathrm{SBII}} v_{\mathrm{SBII}}\left(\sum_i c_{j,\mathrm{SBII}}\frac{d\overline{H}_j^{\mathrm{SBII}}}{dz}\right) + \frac{d}{dz}\left(\tilde{\lambda}_{\mathrm{SBII}}\varepsilon_{\mathrm{SBII}}\frac{dT_{\mathrm{SBII}}}{dz}\right) = 0 \quad (70)$$

Enthalpy balance at SBII-LII interface (annulus flow)

$$\sum_j {}^{\mathrm{LII}}_{\mathrm{SBII}}K_j^0 a_{\mathrm{SBII}}[c_{j,\mathrm{SBII}} - {}^{\mathrm{LII}}_{\mathrm{SBII}}He_j c_{j,\mathrm{LII}}]\overline{H}_j^{\mathrm{SBII}} - \sum_j {}^{\mathrm{LII}}_{\mathrm{SBII}}K_j^0 a_{\mathrm{SBII}}[c_{j,\mathrm{SBII}} - {}^{\mathrm{LII}}_{\mathrm{SBII}}He_j c_{j,\mathrm{LII}}]\overline{H}_j^{\mathrm{LII}} = \dot{h}_{\mathrm{LII}}(T^*_{\mathrm{SBII}} - T_{\mathrm{LII}})a_{\mathrm{SBII}} - \dot{h}_{\mathrm{SBII}}(T_{\mathrm{SBII}} - T^*_{\mathrm{SBII}})a_{\mathrm{SBII}} \quad (71)$$

Enthalpy balance in LI (core flow)

$$-\left(\varepsilon_{\mathrm{LI}} v_{\mathrm{LI}} \sum_j c_{j,\mathrm{LI}} \frac{d\overline{H}_j^{\mathrm{LI}}}{dz}\right) + \frac{d}{dz}\left(\tilde{\lambda}_{\mathrm{LI}} \varepsilon_{\mathrm{LI}} \frac{dT_{\mathrm{LI}}}{dz}\right) - H_{\mathrm{SI}} - h_{\mathrm{wI}} a_{\mathrm{wI}} (T_{\mathrm{LI}} - T_{\mathrm{w}}) - \sum_j {}_{\mathrm{SBI}}^{\mathrm{LI}} K_j^0 a_{\mathrm{SB_I}} [c_{j,\mathrm{SBI}} - {}_{\mathrm{SBI}}^{\mathrm{LI}} He_j c_{j,\mathrm{LI}}] \overline{H}_j^{\mathrm{SBI}} + \sum_j {}_{\mathrm{SBI}}^{\mathrm{LI}} K_j^0 a_{\mathrm{SB_I}} [c_{j,\mathrm{SBI}} - {}_{\mathrm{SBI}}^{\mathrm{LI}} He_j c_{j,\mathrm{LI}}] |\Delta H_{\phi_j}| - \dot{h}_{\mathrm{SBI}} a_{\mathrm{SB_I}} (T^*_{\mathrm{SB_I}} - T_{\mathrm{SBI}}) - \sum_j {}_{\mathrm{LB}}^{\mathrm{LI}} K_j^0 a_{\mathrm{LB}} [c_{j,\mathrm{LB}} - {}_{\mathrm{LB}}^{\mathrm{LI}} He_j c_{j,\mathrm{LI}}] \overline{H}_j^{\mathrm{LB}} + \sum_j {}_{\mathrm{LB}}^{\mathrm{LI}} K_j^0 a_{\mathrm{LB}} [c_{j,\mathrm{LB}} - {}_{\mathrm{LB}}^{\mathrm{LI}} He_j c_{j,\mathrm{LI}}] |\Delta H_{\phi_j}| - \dot{h}_{\mathrm{LB}} a_{\mathrm{LB}} (T^*_{\mathrm{LB}} - T_{\mathrm{LB}}) = 0 \quad (72)$$

with

$$H_{\mathrm{SI}} = \varepsilon_{\mathrm{LSI}} C_{\mathrm{cl}} \left(\Delta H_{\mathrm{WGS}} R^{\mathrm{SI}}_{\mathrm{CO_2}} + \Delta H_{\mathrm{FT}} R^{\mathrm{SI}}_{\mathrm{CO}}\right) \quad (73)$$

Enthalpy balance in LII (annulus flow)

$$-\left(\varepsilon_{\mathrm{LII}} v_{\mathrm{LII}} \sum_j c_{j,\mathrm{LII}} \frac{d\overline{H}_j^{\mathrm{LII}}}{dz}\right) + \frac{d}{dz}\left(\tilde{\lambda}_{\mathrm{LII}} \varepsilon_{\mathrm{LII}} \frac{dT_{\mathrm{LII}}}{dz}\right) - \mathrm{H}_{\mathrm{SII}} - h_{\mathrm{wII}} a_{\mathrm{wII}} (T_{\mathrm{LII}} - T_{\mathrm{w}}) - \sum_j {}_{\mathrm{SBII}}^{\mathrm{LII}} K_j^0 a_{\mathrm{SBII}} [c_{j,\mathrm{SBII}} - {}_{\mathrm{SBII}}^{\mathrm{LII}} He_j c_{j,\mathrm{LII}}] \overline{H}_j^{\mathrm{SBII}} + \sum_j {}_{\mathrm{SBII}}^{\mathrm{LII}} K_j^0 a_{\mathrm{SBII}} [c_{j,\mathrm{SBII}} - {}_{\mathrm{SBII}}^{\mathrm{LII}} He_j c_{j,\mathrm{LII}}] |\Delta H_{\phi_j}| - \dot{h}_{\mathrm{SBII}} a_{\mathrm{SBII}} (T^*_{\mathrm{SBII}} - T_{\mathrm{SBII}}) = 0 \quad (74)$$

with

$$H_{\mathrm{SII}} = \varepsilon_{\mathrm{LSII}} C_{\mathrm{cII}} \left(\Delta H_{\mathrm{WGS}} R^{\mathrm{SII}}_{\mathrm{CO_2}} + \Delta H_{\mathrm{FT}} R^{\mathrm{SII}}_{\mathrm{CO}}\right) \quad (75)$$

Gas phase (SBI, LB, and SBII) boundary conditions

$$\sum_j U_{\mathrm{SB}} \overline{H}_j^{\mathrm{LB}} c_j^{\mathrm{in}} - \left(\sum_j \overline{H}_j^{\mathrm{SBII}} \varepsilon_{\mathrm{SBII}} v_{\mathrm{SBII}} c_{j,\mathrm{SBII}} - \tilde{\lambda}_{\mathrm{SBII}} \varepsilon_{\mathrm{SBII}} \frac{dT_{\mathrm{SBII}}}{dz}\right)_{\mathrm{z=0^+}} = \left(\sum_j \overline{H}_j^{\mathrm{SBI}} \varepsilon_{\mathrm{SBI}} v_{\mathrm{SBI}} c_{j,\mathrm{SBI}} - \tilde{\lambda}_{\mathrm{SBI}} \varepsilon_{\mathrm{SBI}} \frac{dT_{\mathrm{SBI}}}{dz}\right)_{\mathrm{z=0^+}} \quad (76a)$$

$$\left.\frac{dT_{\mathrm{SBI}}}{dz}\right|_{\mathrm{z=H^-}} = 0 \quad (76b)$$

$$\sum_j U_{\mathrm{LB}} \overline{H}_j^{\mathrm{LB}} c_j^{\mathrm{in}} = \left(\sum_j \overline{H}_j^{\mathrm{LB}} \varepsilon_{\mathrm{LB}} v_{\mathrm{LB}} c_{j,\mathrm{LB}} - \tilde{\lambda}_{\mathrm{LB}} \varepsilon_{\mathrm{LB}} \frac{dT_{\mathrm{LB}}}{dz}\right)_{\mathrm{z=0^+}} \quad (77a)$$

$$\left.\frac{dT_{\mathrm{LB}}}{dz}\right|_{\mathrm{z=H^-}} = 0 \quad (77b)$$

$$U_{\mathrm{SB}} \sum_j \overline{H}_j^{\mathrm{SBI}} c_{j,\mathrm{SBI}}\Big|_{\mathrm{z=H^-}} - \left(\sum_j \overline{H}_j^{\mathrm{SBI}} \varepsilon_{\mathrm{SBI}} v_{\mathrm{SBI}} c_{j,\mathrm{SBI}} - \tilde{\lambda}_{\mathrm{SBI}} \varepsilon_{\mathrm{SBI}} \frac{dT_{\mathrm{SBI}}}{dz}\right)_{\mathrm{z=H^-}} = \left(\sum_j \overline{H}_j^{\mathrm{SBII}} \varepsilon_{\mathrm{SBII}} v_{\mathrm{SBII}} c_{j,\mathrm{SBII}} - \tilde{\lambda}_{\mathrm{SBII}} \varepsilon_{\mathrm{SBII}} \frac{dT_{\mathrm{SBII}}}{dz}\right)_{\mathrm{z=H^-}} \quad (78a)$$

$$\left.\frac{dT_{\mathrm{SBII}}}{dz}\right|_{\mathrm{z=0^+}} = 0 \quad (78b)$$

Liquid phase (LI, LII) boundary conditions

$$-\left(\sum_j \overline{H}_j^{\mathrm{LII}} \varepsilon_{\mathrm{LII}} v_{\mathrm{LII}} c_{j,\mathrm{LII}} - \tilde{\lambda}_{\mathrm{LII}} \varepsilon_{\mathrm{LII}} \frac{dT_{\mathrm{LII}}}{dz}\right)_{\mathrm{z=0^+}} = \left(\sum_j \overline{H}_j^{\mathrm{LI}} \varepsilon_{\mathrm{LI}} v_{\mathrm{LI}} c_{j,\mathrm{LI}} - \tilde{\lambda}_{\mathrm{LI}} \varepsilon_{\mathrm{LI}} \frac{dT_{\mathrm{LI}}}{dz}\right)_{\mathrm{z=0^+}} \quad (79a)$$

$$\left.\frac{dT_{\mathrm{LI}}}{dz}\right|_{\mathrm{z=H^-}} = 0 \quad (79b)$$

$$-\left(\sum_j \overline{H}_j^{\mathrm{LI}} \varepsilon_{\mathrm{LI}} v_{\mathrm{LI}} c_{j,\mathrm{LI}} - \tilde{\lambda}_{\mathrm{LI}} \varepsilon_{\mathrm{LI}} \frac{dT_{\mathrm{LI}}}{dz}\right)_{\mathrm{z=H^-}} = \left(\sum_j \overline{H}_j^{\mathrm{LII}} \varepsilon_{\mathrm{LII}} v_{\mathrm{LII}} c_{j,\mathrm{LII}} - \tilde{\lambda}_{\mathrm{LII}} \varepsilon_{\mathrm{LII}} \frac{dT_{\mathrm{LII}}}{dz}\right)_{\mathrm{z=H^-}} \quad (80a)$$

$$\left.\frac{dT_{\mathrm{LII}}}{dz}\right|_{\mathrm{z=0^+}} = 0 \quad (80b)$$

Thermodynamic model, property, and data correlations

Vapor-liquid equilibria (VLE) play an important role in the production of hydrocarbons via FTS, especially when the reaction is carried out in a three-phase slurry reactor. At reaction conditions, the FTS products distribute between the SBCR vapor and liquid phases. The lighter components desorb and are carried with unreacted syngas while the heavier ones preferentially reside in the liquid. Reactor performance is strongly dependent on the composition of the liquid phase which affects both the synthesis chemistry and the reactor hydrodynamics.[46,47] The VLEs at the vapor–liquid interfaces and related mass-transfer limitations determine the compositions in the different compartments of the reactor. Therefore, the compositions at the liquid and vapor sides of the interfaces are evaluated using VLE flash calculations at the interfacial temperatures corresponding to the contiguous vapor and liquid compartments (SBI-LI, LB-LI, and SBII-LII). The Peng-Robinson/Marano-Holder thermodynamic model[46,47] was used as briefly explained later.

The j-species vapor-phase fugacity coefficient, $\phi_{j,\mathrm{v}}$, is estimated with the Peng–Robinson equation of state to yield the vapor-phase fugacity:

$$f_{j,v} = \phi_{j,v} y_j P \quad (81)$$

where y_j is the vapor-phase mole fraction and P, the pressure.

The liquid-phase fugacity for nonhydrocarbon gases and for C_1 to C_3 hydrocarbons is calculated from the following expression:

$$f_{j,\mathrm{L}} = H_j^{\infty} x_j \exp[\overline{V}_j^{\infty}(P - P_{j,\mathrm{sat}})/RT] \tag{82}$$

where H_j^{∞} is the Henry's constant at infinite dilution, x_j the liquid-phase mole fraction, $\overline{V}_j^{\infty}$ the partial molar volume at infinite dilution, and $P_{j,\mathrm{sat}}$ is the vapor pressure of saturated pure j component at the equilibrium temperature T.

For the C_{4+} components, an activity coefficient, γ_j^{∞}, is defined as:

$$\gamma_j^{\infty} = H_j^{\infty}/P_{j,\mathrm{sat}} \tag{83}$$

and their corresponding liquid fugacity writes, after substitution of Eq. 83 in Eq. 82, as:

$$f_{j,\mathrm{L}} = \gamma_j^{\infty} P_{j,\mathrm{sat}} x_j \exp[\overline{V}_j^{\infty}(P - P_{j,\mathrm{sat}})/RT] \tag{84}$$

On the basis of lattice fluid theory,[48] $\ln H_j^{\infty}$ is asymptotically linear with solute carbon number m. The asymptotic behavior of $\ln P_{j,\mathrm{sat}}$ is also linear with m.[47] Therefore, from Eq. 83, $\ln \gamma_j^{\infty}$ is also asymptotically linear with m. Thus, it is possible to estimate $\ln \gamma_j^{\infty}$ for higher-carbon-number normal paraffin solutes in a normal paraffin solvent based on experimental data or correlations for a given reference solute, with carbon number r, in the same solvent:

$$\ln \gamma_{\mathrm{m}}^{\infty} = \frac{n-m}{n-r} \ln \gamma_{\mathrm{n}}^{\infty} \tag{85}$$

For estimating the infinite-dilution activity coefficients of C_{4+} components, n-C_6H_{14} was used as the reference solute.

To perform the specified P-T-flash calculations, the following properties are required: the critical pressures, temperatures and acentric factors for all components; the Henry's constants and partial molar volumes at infinite dilution for H_2, CO, CO_2, H_2O, N_2, CH_4, C_2H_4, C_2H_6, C_3H_6, C_3H_8, and n-C_6H_{14} (reference solute) in n-paraffin solvents; and vapor pressures and liquid molar volumes for all α-olefins and C_{4+} n-paraffins. Due to lack of data, the following assumptions were used: the partial molar volume of N_2 is approximated with that of CO. For H_2O, the partial molar volume is based on the correlation of saturated-liquid data obtained from steam tables. For C_3H_6 and C_3H_8, pure liquid molar volumes are used. Critical properties, vapor pressures, liquid molar volumes, and Henry's constants for n-paraffins and α-olefins were estimated using the asymptotic behavior ABC correlation developed by Marano.[46] For the other pure components used in the flash calculations, the critical properties were obtained from Reid et al.[49]

The liquid and ideal-gas heat capacities, the enthalpies of formation, and the enthalpies of vaporization of the n-paraffins and α-olefins were estimated with the ABC correlations developed by Marano and Holder.[46,47] The temperature correction of the enthalpies of vaporization was done following Reid et al.[49] recommendation. For the other species present in the liquid and gas mixtures, the heat capacities were estimated with polynomial correlations from Reid et al.[49]

The conductive heat transfer coefficients at the interfaces were estimated using a Chilton–Colburn analogy between the mass and heat transfers.[45] The Ackermann correction was used to take into account the convective effects in the thermal boundary layers.[45] However, the final version of the heat transfer coefficients at the interfaces, $\dot{h}_x$ (x = SBI, SBII, LB, LI, LII), was simplified because the Ackermann correction gave negligible corrective values.

The thermal conductivity of the gaseous components was estimated using the correlation of Chung et al. while the thermal conductivity of the gas mixture was deduced using the Wassiljewa equation.[49] The liquid thermal conductivity of each n-paraffin and α-olefin component was estimated with the Marano and Holder ABC correlations[46,47] and the liquid-mixture thermal conductivity was evaluated using the Li equation.[49] For the other species present in the reaction mixture, the thermal conductivity was estimated using appropriate correlations from Reid et al.[49]

The heat transfer coefficients at the wall, h_{wI} and h_{wII}, were estimated using the surface renewal model proposed by Deckwer et al.[50] In addition, we needed to develop a set of constitutive equations for the estimation of the turbulent thermal conductivity of the liquid and gas phases. As for the estimation of $\tilde{k}$ and D_{s}, these equations are based on the Kolmogorov's isotropic turbulence theory. Full details unveiling these derivations will be provided in a future work:

$$\tilde{\lambda}_{\mathrm{g(L)}} = \frac{12.6(5^{5/3}-1)}{620} \rho_{\mathrm{g(L)}} \overline{C}_{\mathrm{p}}^{\mathrm{g(L)}} d_{\mathrm{LB}} \sqrt[3]{g d_{\mathrm{LB}} U_{\mathrm{g}}} \tag{86}$$

$$\mathrm{g} = \mathrm{SBI},\ \mathrm{SBII};\ \mathrm{L} = \mathrm{LI},\ \mathrm{LII}$$

$$\tilde{\lambda}_{\mathrm{LB}} = 1.4 \rho_{\mathrm{LB}} \overline{C}_{\mathrm{p}}^{\mathrm{LB}} d_{\mathrm{LB}} \sqrt[3]{g d_{\mathrm{LB}} U_{\mathrm{g}}} \tag{87}$$

The liquid-side mass transfer coefficients were estimated with the correlations proposed by Maretto and Krishna[7] where the liquid diffusivity coefficients were estimated with the Wilke-Chang or Olander correlations.[49] The gas-side mass transfer coefficients were evaluated using appropriate correlations for k_{G} with rigid interfaces (small bubbles, SBI, SBII), or laminar or turbulent flow k_{G} for the LB.[45] Finally, the liquid–solid mass transfer coefficients were estimated with a correlation proposed by Sanger and Deckwer.[51]

Fischer–Tropsch synthesis and water gas shift kinetics

Fischer–Tropsch Intrinsic Kinetics. The kinetics of the Fischer–Tropsch reaction with cobalt-based catalysts has been studied by many investigators[9,52–58] and it has been shown that cobalt-based catalysts, in general, outperform iron-based catalysts especially in terms of catalyst life. It has been realized that α-olefins produced in FTS reactions can readsorb on the catalyst surface and further take part in the polymerization reactions. A detailed intrinsic kinetics model accounting for α-olefin readsorption has been developed by Anfray[58] and is used in this work to describe the n-paraffin and the α-olefin formation using a cobalt catalyst. Details on the catalytic system can be found in Bremaud et al.[59] and Anfray et al.[60] The consumption and formation rates are based on nondissociative CO adsorption mechanism.[55,58] The main expressions for the kinetic rates are summarized in Appendix B and the numerical values of the different parameters can be taken from the work of Anfray et al.[58,60] An activation energy of 100 kJ/mol was assumed to take into

account the variation with temperature of the Fischer–Tropsch intrinsic kinetics. The Fischer–Tropsch consumption and formation rates were estimated as a function of their values at 493 K:

$$R_{j,T} = R_{j,T=493\mathrm{K}} \exp[100{,}000/R(1/493 - 1/T)] \tag{88}$$

Water Gas Shift Intrinsic Kinetics. Though the water gas shift activity of cobalt-based catalysts is not dominant, it is worth examining especially from the point of view of reactor thermicity as the selectivity towards CO_2 may increase with temperature diverting a portion of useful CO especially at high CO conversion. In this study, it was assumed that the FTS and the WGS ($CO + H_2O \rightarrow CO_2 + H_2$) reactions occur on different active sites with no interactions between the respective surface reactions.[61] The presence of WGS reaction with cobalt catalyst was accounted for by using a kinetic model developed by Keyser et al.[61] (Appendix C). R_{WGS} in Eq. C.1 was added to Eq. B.1 to calculate the net CO consumption. Similarly, it was rested from Eq. B.2 to account for the hydrogen produced. In addition, the CO_2 selectivity was calculated with the following expression:

$$\mathrm{CO_2\ selectivity} = \frac{v_{\mathrm{SB_I}}\varepsilon_{\mathrm{SB_I}}C_{\mathrm{CO_2,SB_I}}|_{z=H} + v_{\mathrm{SB_{II}}}\varepsilon_{\mathrm{SB_{II}}}C_{\mathrm{CO_2,SB_{II}}}|_{z=H} + v_{\mathrm{LB}}\varepsilon_{\mathrm{LB}}C_{\mathrm{CO_2,LB}}|_{z=H}}{U_g C_{\mathrm{CO}}^{\mathrm{in}} - (v_{\mathrm{SB_I}}\varepsilon_{\mathrm{SB_I}}C_{\mathrm{CO,SB_I}}|_{z=H} + v_{\mathrm{SB_{II}}}\varepsilon_{\mathrm{SB_{II}}}C_{\mathrm{CO,SB_{II}}}|_{z=H} + v_{\mathrm{LB}}\varepsilon_{\mathrm{LB}}\varepsilon_{\mathrm{LB}}C_{\mathrm{CO,LB}}|_{z=H})} \tag{89}$$

Results and Discussion

The Aspen Custom Modeler software was used to generate the numerical platform needed for solving the mixed algebraic-ODE system of equations of the hydrodynamic model coupled with the species and the enthalpy balance equations for the FTS SBCR. A 1st-order backward finite difference method in the radial direction and a 2nd-order backward finite difference method for the axial direction were used for the discretization in the hydrodynamic unit. In the other units of the numerical platform, discretization in the axial direction was realized using 2nd-order central finite difference method. A nonlinear solver based on the Newton method was used to solve the set of simultaneous model equations.

Brief analysis of the sedimentation/advection/dispersion/lateral exchange model

A series of simulations in cold-flow passive conditions was first carried out to assess the necessity of bringing a detailed description of slurry-phase turbulence on the one hand, and of the dispersive terms in the catalyst transport equations (2nd-order terms in ODEs, Eqs. 25 and 26), on the other hand.

Note that the philosophy of our proposed sedimentation model is quite different from the conventional sedimentation models used in the literature because it explicates the role of the advective transport of catalyst in the logic of the core-annulus flow structure. Besides, we refrained from using literature correlations for estimating the dispersion coefficient of the solid phase derived from an analysis of the classical sedimentation/dispersion models. As a matter of fact, the order of magnitude predicted from these correlations is generally high, often from 0.1 and 1 m^2/s.[62] This is well above the typical magnitude of experimentally measured eddy diffusivity coefficients for the solids in slurry bubble columns as reported by Rados[40] who determined D_s values using a computer-aided radioactive particle tracking technique. The reason for it is that the D_s values interpreted using classical (batch-wise) sedimentation/dispersion mass balance equations are flawed by the absence of an adequate term accounting for the gas-induced advective recirculation of the solids. Instead, the tepid contribution from the sedimentation term left in these models is far from reflecting the true kinematics of the catalyst in SBCR. Fortunately, the D_s values calculated from our simplified isotropic turbulence model (Eq. 43) were close to those measured by Rados.[40] We will therefore rely on the D_s estimations from Eq. 43 in the next simulations. In our view, the proposed model represents a complete formulation which is capable of providing order-of-magnitude comparisons of the advective and dispersive transport terms of catalyst in SBCR.

The simulated conditions summarized in Table 1 correspond to typical experimental conditions reported in the literature for SBCR.[11–14,25–64] Figure 3 presents computed longitudinal profiles of the catalyst concentration in the core region as a function of z/H for the four cases:

- Second-order sedimentation/advection/**dispersion**/lateral exchange model (axial dispersion, AD) with shear-induced turbulence model using the Prandtl–Nikuradse mixing length.
- Second-order sedimentation/advection/**dispersion**/lateral exchange model (axial dispersion, AD) with combined shear-induced and bubble-induced turbulence model in the slurry phase.
- First-order sedimentation/advection/lateral exchange model (plug flow, PF) with shear-induced turbulence model using the Prandtl–Nikuradse mixing length.
- First-order sedimentation/advection/lateral exchange model (plug flow, PF) with combined shear-induced and bubble-induced turbulence model in the slurry phase.

The main conclusions drawn from the comparison of the four simulation scenarios are as follows:

- The second-order sedimentation/advection/**dispersion**/lateral exchange model brings no significant gain with respect to a first-order sedimentation/advection/lateral exchange model. Hence, purely advective transport of catalyst can largely be sufficient to explain the axial distribution of catalyst in SBCR.
- The simplest of liquid turbulence models is sufficient to reproduce the catalyst concentration profiles. This however seems not surprising as Sokolichin et al.[65] have already shown that the simplest model accounting for the bubble influence on the slurry turbulence is due to Sato et al.[35] which models the effective viscosity, as aforementioned, as a shear induced term and a bubble induced term. Sokolichin et al.[65] have found that in the homogeneous bubbly flow

Table 1. Simulated Conditions Used for Analysis of the Hydrodynamic Model in Passive Conditions

	Parameters						
Reference	U_g (m/s)	ρ_p^* (kg/m^3)	ρ_g (kg/m^3)	D (m)	H (m)	C_{c0} (kg/m^3)	d_p (μm)
Gandhi et al.[63]	0.26	2452	1.29	15	1.05	77.2	35
Kato et al.[64]	0.082	2520	1.29	6.6	2.01	100	88
Rados[40]	0.140	2490	1.29	16	1.78	226.6	131
O'Dowd et al.[62]	0.081	2420	1.29	10.8	1.94	244	90

*ρ_p represents the bulk particle density expressed on a dry basis [kg solids/m^3 of particle (skeletal + porous volumes)].

regime, the bubble-induced viscosity is nearly two orders of magnitude smaller than the shear-induced turbulent viscosity. As Figures 3–6 show, it is likely that for the gas velocity conditions simulated in our work, the turbulence model of Sato et al.[35] still provides insufficient ameliorations with respect to a simple shear-induced turbulent model such as the Prandlt–Nikuradse model.

Isothermal simulations

This section presents the simulation results for the isothermal case. The operating conditions and geometry of the reactors are listed in Table 2. The simulations were conducted bearing in mind two features relevant for the industrial context of FTS: (i) the gas superficial velocities correspond always to the churn turbulent flow regime, (ii) the vessel sizes (height and diameter) are compatible with commercial-scale SBCR units.

Figure 4 shows the influence of temperature on the CO and H_2 conversion with and without inclusion of the WGS, and assuming first a negligible variation of gas superficial velocity due to chemical contraction. Increasingly reactor temperatures expectably translate into higher CO and H_2 conversions at the reactor exit. Accounting for the WGS reaction increases the CO consumption rates thereby increasing CO conversions. Hydrogen consumption by the FTS reactions is counterbalanced by hydrogen production due to the WGS reaction. However, H_2 conversions appear to be marginally influenced by the WGS reaction. The slight unexpected increase in hydrogen conversion when the WGS is enabled could be explained by the fact that the FTS reaction rates are boosted by the hydrogen local over-concentration due to WGS at the catalyst sites, entraining a further CO consumption coherent with the larger contrasts in CO conversion between enabled and disabled WGS, see Figure 4a.

In Figure 4, the gas superficial velocity was considered constant and equal with the inlet value. Superficial gas veloc-

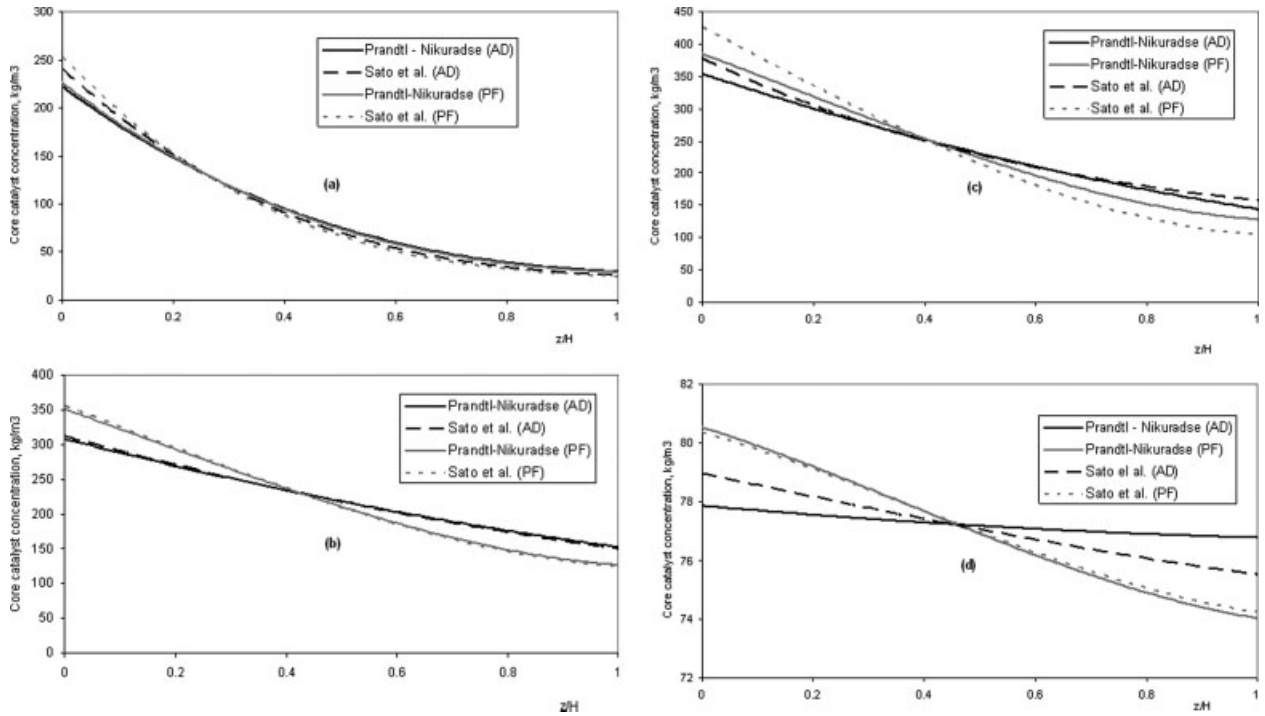

Figure 3. Simulation of catalyst distribution in SBCR for the conditions studied by (a) Kato et al.[64] (b) Rados[40] (c) O'Dowd et al.[62] (d) Gandhi et al.[63]

Assessment of the effect of the choice of turbulence model, and dispersive versus advective transport of catalyst.

Table 2. Summary of SBCR Simulation Conditions–Isothermal Case

SBCR diameter	7–11 m	Inlet gas superficial velocity	0.2–0.35 m/s
SBCR height	28–42 m	Inlet gas density	6.3–6.5 kg/m^3
Catalyst concentration	215–300 kg/m^3	Operating pressure	25 bar
Dry catalyst bulk density	850 kg/m^3	Temperature range	230–245°C
Solids volume fraction (per unit slurry volume)	0.25–0.35		

ity directly affects the gas mean residence time and thus reactor performance. Therefore, reliable calculation of a change in superficial gas velocity is important for proper prediction of reactor performance. The change in gas flow rate was calculated from the overall mass balance equation (Eq. 65) that accounts for both the small bubbles SBI and SBII, and the LB. Figures 5 and 6 show that CO and H_2 conversions are indeed sensitive to gas phase contraction effects. Had the correction on local superficial velocity been applied, the conversions of CO and hydrogen were systematically larger because of the longer residence times of the reactants.

Figure 7 shows the effect of catalyst concentration on the CO and H_2 conversions under variable gas superficial velocity conditions. Increasing catalyst concentration improves CO and H_2 conversions. Increasing the catalyst inventory by 40% translates in about 65% improvement in CO conversion from $\varepsilon_s = 0.25$ to 0.35. Note that the influence of catalyst holdup is not only a positive effect in terms of reaction, but also a detrimental effect on the total gas holdup which undergo a decreasing trend as the solids holdup is increased.[23]

Figure 8 shows the influence of temperature on CO and H_2 conversions along with CO_2 selectivity for two values of inlet gas superficial velocity. As expected, CO and hydrogen conversions decrease with increasing inlet gas superficial velocity. When the WGS reaction is enabled in the simulator, the CO_2 selectivity is also increasing with increased CO conversions. In addition, the order of magnitude regarding CO_2 selectivity is consistent with the experimental results reported by Keyser et al.[61]

The cobalt catalyst produces especially paraffins. Figure 9a shows the distribution of the paraffins in the liquid phase at the column exit ($T = 220$°C). According to simulation results, the average carbon number of Fischer–Tropsch wax is 29 ($H_2/CO = 2.15$, $U_{g,in} = 0.3$ m/s). This is in good agreement with the experimental results obtained by Anfray.[58] For the cobalt catalyst and the simulated conditions, the liquid concentration of olefins is typically an order of magnitude lesser than their paraffin counterparts up to C_{15} as can be seen in Figure 9b. The decline in the concentrations in olefins higher than C_{15} is even more pronounced and so continues below the 0.001 mol/L level shown in Figure 9b.

Nonisothermal simulations

This section briefly discusses some simulation results for the nonisothermal case. The operating conditions and geometry, including the installed heat exchange area, of the SBCR are listed in Table 3. The simulations are shown for the case where an intense lateral mass transfer takes place between the core small bubbles SBI and LB to allow homogenization of the species compositions within the two bubble classes. A value for the mass transfer coefficient $k_{SBI–LB}$ equal to 350 was chosen to force the same compositions in both bubble classes. Note that this coefficient is a convenient phenomenological means to modulate the species compositions in the small and LB classes as a result of complete or partial equilibrium between bubble coalescence and breakup rates.

Figure 10 shows the axial temperature profiles at steady-state operation in the different gas and liquid phase compartments. WGS reaction is enabled, and the inlet gas temperature is taken equal to the wall temperature imposed to the heat exchange area in charge of the heat removal out of the

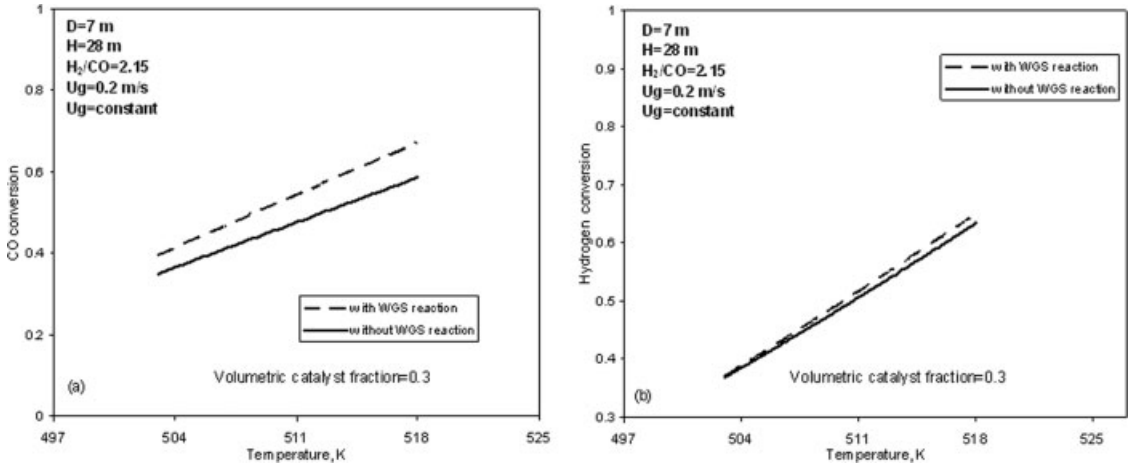

Figure 4. Influence of operating temperature on CO (a) and H_2 (b) conversion in the presence and absence of WGS reaction (gas contraction neglected).

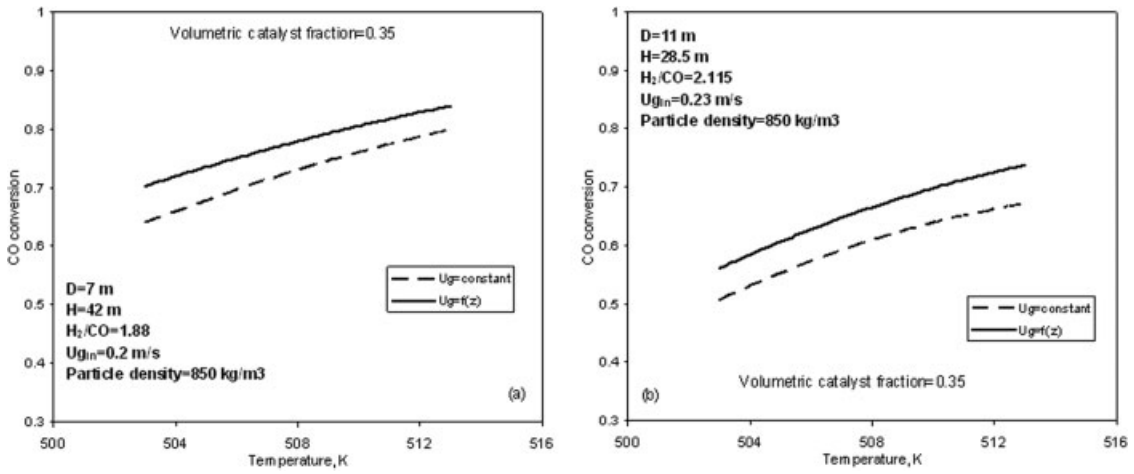

Figure 5. Influence of operating temperature on CO conversion under constant and variable gas velocity conditions for two H_2/CO ratios (a) $H_2/CO = 1.88$, $U_{gin} = 0.2$ m/s, (b) $H_2/CO = 2.115$, $U_{gin} = 0.23$ m/s.

SBCR, i.e., $T_{g,in} = T_w = 500$ K. It can be seen that the temperature contrast between SBII and LII phases in the annulus region is barely perceptible and can be explained by the lower gas capacity associated with the lower gas flux in the wall region which is being heated up pretty rapidly by a hotter liquid LII. For these simulation conditions, the temperature in the liquid compartments LI and LII is nearly uniform despite a tiny dip towards the reactor exit. The temperature differences between the core and the annulus gas phases were found to increase with an increase in wall temperature (results nor shown). The nonisothermal simulations reveal also that inasmuch as heat removal is well managed from the heat exchange area, the reactor operation can be considered as nearly isothermal. This provides *post facto* justification of SBCR for FTS owing to the superiority of their heat removal capability.

Sensitivity analysis of the simulations

The simulation trends revealed by the proposed model can be valuable only if the model can instruct us on how the figures put for the estimation of a whole constellation of hydrodynamic, heat and mass transfer parameters needed in it are to have repercussions on the simulated performances of SBCR units. This exercise is obviously impossible to validate *a priori* for commercial-scale simulations. It remains nonetheless highly desirable for engineers whose goal is to tailor the most robust and simpler design model while only keeping minimal physics in it for scale up purposes. This approach supposes that model complexity can be rationally degraded by retaining, among the larger reservoir of physical and chemical features contained in the original model, only those features that are identified to noticeably affect the simulated model performance. An obvious approach would be to perform a sensitivity analysis to study the influence of hydrodynamic, mass and heat transfer parameters on the reactor performance.

Accessibility in the open literature of these parameters relevant to SBCR commercial-size being impossible, it would be difficult to discuss the sensitivity analysis with full knowledge. Rather, we preferred to perform a sensitivity analysis

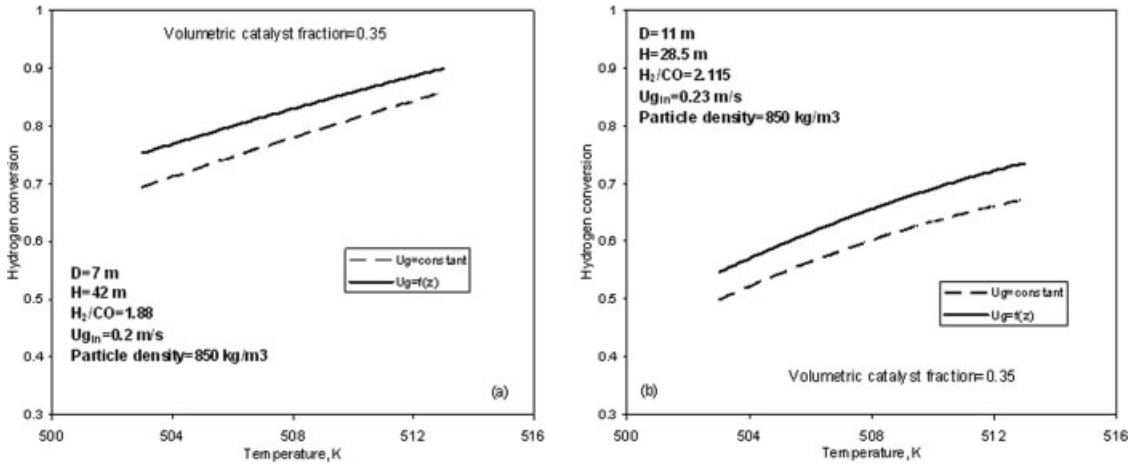

Figure 6. Influence of operating temperature on H_2 conversion under constant and variable gas velocity conditions for two H_2/CO ratios (a) $H_2/CO = 1.88$, $U_{gin} = 0.2$ m/s, (b) $H_2/CO = 2.115$, $U_{gin} = 0.23$ m/s.

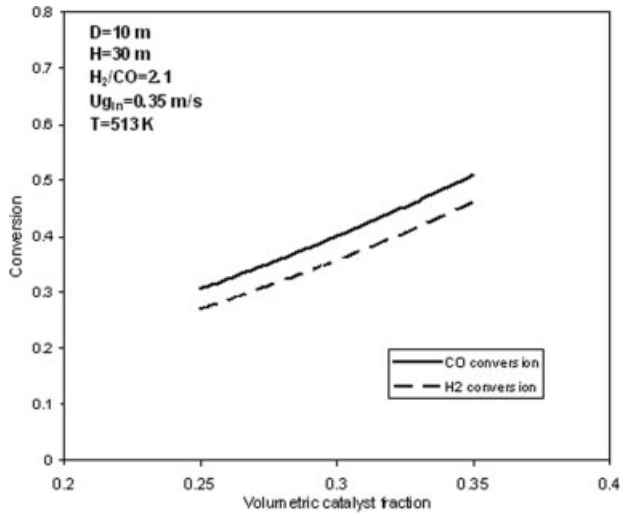

Figure 7. CO and H_2 conversion as a function of catalyst holdup (expressed on the basis of slurry volume).

for a smaller-scale base-case SBCR where accessible information and confident mass and heat transfer data and correlations are less venturous. The diameter and height of the base SBCR were set to 0.46 and 4.6 m, and the superficial gas velocity was varied between 0.2 and 0.3 m/s, and the catalyst fraction was varied between 0.2 and 0.35.

At low values of LB-SBI interaction cross-flow coefficient, k_{SBI-LB}, the concentration of the gas reactants is smaller in SBI than in LB because of the larger interfacial area that is available for mass transfer between SBI and LI. A large amount of unreacted CO and hydrogen that are present in LB in this case practically would bypass the reactor because the unit volume area available for LB-LI mass transfer is much lower than that for SBI-LI mass transfer. At high k_{SBI-LB} values, bubble coalescence and breakup rates reach equilibrium yielding gas concentration profiles similar in SBI and LB compartments. However, even if LB–SBI interaction cross-flow coefficient was found to affect significantly the gas reactants concentration profiles in LB and SBI, CO and H_2 conversions were not significantly influenced by this parameter. Therefore, knowing accurately this parameter is not critical for the assessment of global conversions in SBCR. Approximate values taken from experimental CARPT measurements for example would be sufficient, see Gupta et al.[33]

Regarding the mass exchange coefficient between the small bubble compartments SBI and SBII, a twofold increase and a 10-fold reduction of $\tilde{k}$ with respect to the base case value-calculated with the isotropic turbulence model, Eq. 42 were considered. Higher $\tilde{k}$ values result in higher mass flux transported between SBI and SBII and tend to increase the gas reactant concentrations in the SBII compartment. This in turn enhances the reaction rates in the contiguous LSII slurry resulting in a higher liquid temperature in the annulus. However, even if $\tilde{k}$ values affect both the gas reactant concentration profiles in SBII and temperature profiles, the CO and H_2 conversions and the hydrocarbon concentration in the liquid phase remained marginally influenced in the range [0.1–2 $\tilde{k}$] of the nominal value corresponding to the base case value.

Gas–liquid mass transfer coefficients were evaluated with the correlations proposed by Maretto and Krishna.[7] A fivefold increase or a 1.5-fold reduction of the gas-liquid mass transfer coefficient with respect to the base case value was considered. The reactor performance was found to be significantly affected by the gas–liquid mass transfer coefficient and an accurate model to describe the gas–liquid mass transfer would be vital. As expected, gas reactant conversions increase with an increase in the gas–liquid mass transfer coefficient because of the higher mass transfer flux transported between gas and liquid phases.

The liquid–solid mass transfer coefficients were evaluated with the correlations proposed by Sanger and Deckwer.[51] A 10-fold increase or a 10-fold reduction of the liquid–solid mass transfer coefficient with respect to the base case value was considered. The reactor performance remained insensitive to the liquid–solid mass transfer coefficients varied in the above range. Owing to the high surface area of suspended catalyst, the resistance at the liquid–solid surface, if any, can be neglected even for the lower limit of liquid–solid mass transfer coefficient.

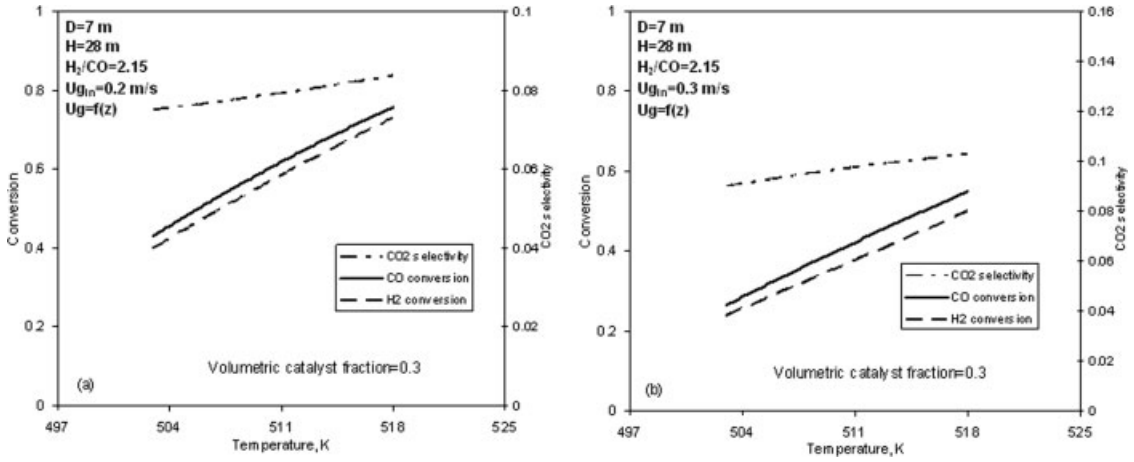

Figure 8. Influence of operating temperature, gas inlet superficial velocity on CO and H_2 conversion and CO_2 selectivity under variable gas velocity conditions. (a) U_{gin} = 0.2 m/s, (b) U_{gin} = 0.3 m/s.

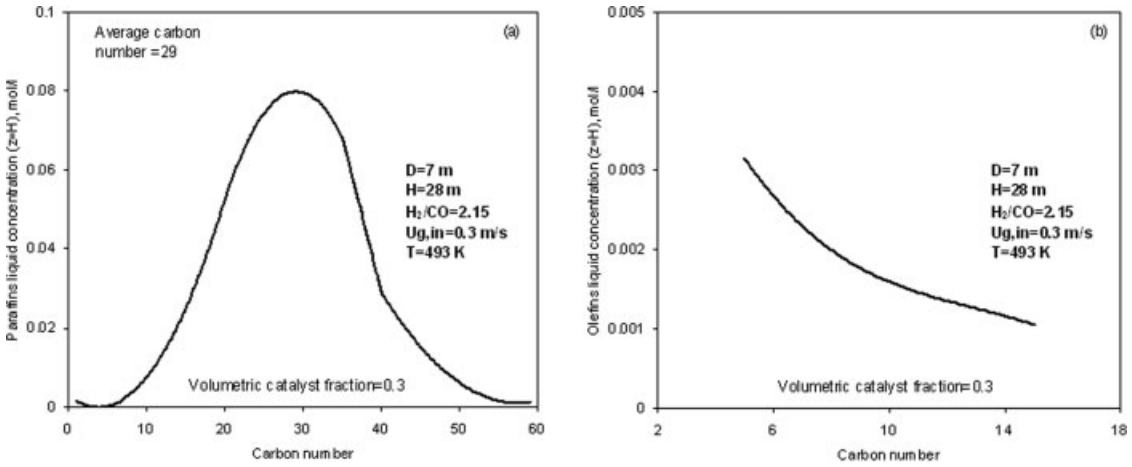

Figure 9. Paraffins (a) and olefins (b) distributions in the liquid phase at the SBCR exit height.

Table 3. Summary of SBCR Simulation Conditions–Nonisothermal Case

SBCR diameter	7 m	Inlet gas superficial velocity	0.3 m/s
SBCR height	28 m	Inlet gas density	6.5 kg/m^3
Catalyst concentration	255 kg/m^3	Operating pressure	25 bar
Dry catalyst bulk density	850 kg/m^3	Inlet gas and wall temperature	227°C
Solids volume fraction (per unit slurry volume)	0.3	Heat transfer area	10 m^2/m^3

CO and H_2 conversions were found also to be weakly responsive to changes of the mass transfer coefficient between core and annulus liquid, i.e., LI–LII lateral mixing. This was verified for a 2-fold increase or a 10-fold reduction of the LI–LII mass transfer coefficient with respect to the base case value-calculated with the isotropic turbulence model, Eq. 42.

Reactor performance is also strongly dependent on the wall heat transfer coefficient. The heat transfer at the wall was estimated using the surface renewal model developed by Deckwer et al.[50] The increase of the wall heat transfer coefficient improves the heat transfer towards the exterior of the SBCR, results in a lower temperature inside the reactor and consequently in lower CO and H_2 conversions. The same effects are obtained when the heat transfer area is increased or the wall temperature is decreased. There is hence a large degree of freedom with regard to the adjustment of the reactor temperature.

A 10-fold increase or a 2-fold reduction of the heat transfer coefficient at the gas–liquid interface with respect to the base case value -calculated with the Chilton–Colburn analogy[45] was considered. High values of heat transfer coefficient increase the interfacial heat flux transported between the liquid and the gas phases yielding higher gas temperatures. Nonetheless, the difference between SBII and LII temperatures was lower because of the lesser gas holdup in the

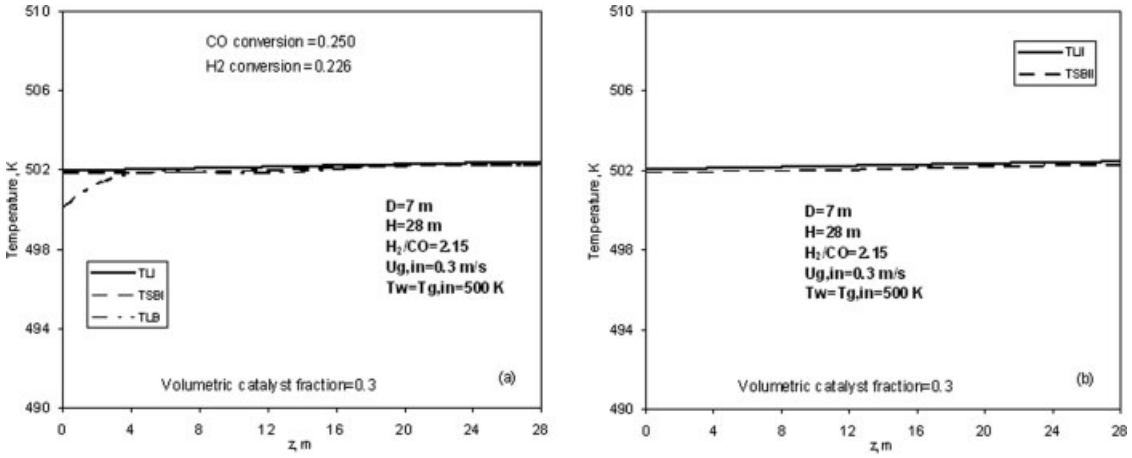

Figure 10. Axial variations of the gas and liquid temperatures within the various SBCR compartments using the nonisothermal version of the SBCR model.

annulus region. In addition, the greater differences between LB and LI temperatures could be explained by the lower interfacial area between them.

The conversions of CO and H_2 depend on the H_2/CO feed mole ratio. CO exerts an inhibiting effect on the FTS, contrarily to H_2 which accelerates reaction. A low H_2/CO feed ratio slows down CO and H_2 consumption rates which consequently lower the CO and H_2 overall conversions. Conversely, high H_2/CO feed ratios improve CO and H_2 overall conversions. However, high H_2/CO ratios favor the production in high quantity of light *n*-paraffins because of favored H_2 adsorption and dissociation, and thereafter hydrogenation of hydrocarbon chains. In this regard, our simulations were coherent with the findings of Anfray.[58]

Finally, the influence of pressure on the reactor performance was analyzed. It was found that increasing the reactor pressure, and thus reactant solubilities, yielded increased liquid temperatures, and higher conversion rates.

Conclusion

A comprehensive multicomponent, core-annulus multicompartment pseudo 2D two-bubble class model for FTS SBCR was developed. The model consisted of a detailed hydrodynamic platform where upon were tied the Fischer–Tropsch and the water-gas-shift catalytic reactions, the descriptions of thermodynamics and thermal effects, the variable gas flow rate due to chemical/physical contraction, and the gas and slurry (re)circulation and intra-phase per-compartment backmixing. The following conclusions were drawn from the simulation results of the study:

- The dispersion term of the catalyst transport equations brought no significant gain with respect to the axial distribution of the catalyst in SBCR. Purely advective catalyst transport equations taking account of sedimentation and lateral exchange were sufficient to represent axial catalyst profiles.
- Inclusion of the Sato et al.[35] bubble-induced turbulence model did not show significant changes with respect to the use of simpler Prandtl–Nikuradse mixing-length shear-induced turbulence model.
- Sensitivity analysis showed that the most critical parameter was the gas–liquid mass coefficient.
- The LB–SBI and the SBI–SBII cross-flow mass transfer coefficients, though they affected the specie axial concentration profiles in the gas compartments, influenced only marginally the overall reactor conversion.
- Space-dependent superficial gas velocity directly affects the mean gas residence time, and so temperature and CO conversions were influenced by the actual local gas velocity. Reliable estimation of the gas velocity due to chemical contraction is critical when conversion exceeds 50%.
- Temperature and CO conversions were found to depend in some extent on the water gas shift reaction and exhibited variations coherent with general wisdom.

Acknowledgments

Drs. S. Savin, J. Bousquet and F. Luck are greatly acknowledged for the fruitful discussions on the Fischer-Tropsch process. The help of D. Desvigne in the preliminary developments of the hydrodynamic platform is acknowledged with gratitude.

Notation

a_e = CO consumption rate constant, m^6/s kg kmol
a_{LSi} = liquid–solid mass transfer area, m^2/m^3 reactor
a_{LB} = gas(LB)-liquid (LI) mass transfer area, m^2/m^3 reactor
a_{SBI} = gas(SBI)-liquid (LI) mass transfer area, m^2/m^3 reactor
a_{SBII} = gas(SBII)-liquid (LII) mass transfer area, m^2/m^3 reactor
a_{wi} = heat transfer area, m^2/m^3 reactor
b_e = inhibition CO consumption rate constant, m^3/kmol
c = parameter
$c_{j,i}$ = concentration of species j in compartment i, kmol/m^3_i
$c^s_{j,i}$ = concentration of the species j at the catalyst surface, kmol/m^3_i
C_{c0} = average mass catalyst concentration, kg/m^3 slurry
C_{ci} = mass catalyst concentration in i compartment, kg/m^3 slurry
$\overline{C}_p^{g(L)}$ = mass heat capacity of gas (liquid) phase, J/kg K
$\overline{C}_p^{LB}$ = mass heat capacity of large bubbles phase, J/kg K
C_t = concentration of catalytic sites, kmol/m^3
C_D = drag coefficient, −
C_G = total concentration in gas phase, kmol/m^3
d = local bubbles diameter, m
d_i = average bubbles diameter in i (SBI, SBII, and LB) compartment, m
d_p = catalyst particle diameter, m
D = reactor diameter, m
D_s = axial dispersion coefficient in the solid phase, m^2/s
D_{LB} = axial dispersion coefficient in large bubbles compartment, m^2/s
Eo = Eotvos number, Eo = $\frac{d^2(\rho_{ls}-\rho_g)g}{\sigma}$
$f_{j,L}$ = liquid-phase fugacity for component j in solution
$f_{j,v}$ = vapor-phase fugacity for component j
g = gravitational acceleration, m/s^2
h_i = heat transfer coefficient at the gas–liquid interface, J/m^2 s K
h_{wi} = heat transfer at the wall, J/m^2 s K
H = reactor length, m
H_j^∞ = Henry's constant at infinite dilution, bar
${}^k_iHe_j$ = Henry constant of species j, m^3_l/m^3_g
$\overline{H}^i_j$ = molar enthalpy of species j in the compartment i, kJ/kmol
k = mixing length constant
$\tilde{k}$ = mass transfer coefficient at the core-annulus interface, m/s
k_{*C1} = C1 formation rate constant, m^6/s kg kmol
k_1 = empirical constant
k_j^{LS} = liquid–solid mass transfer coefficient of species j, m/s
k_a = α-olefins re-adsorption constant rate, m^6/s kg kmol
k_p = propagation rate constant, m^6/s kg kmol
k_{tp} = paraffins desorption rate constant, m^6/s kg kmol
$k_{tp,1}$ = methane desorption rate constant, m^6/s kg kmol
k_{to} = α-olefins desorption rate constant, m^6/s kg
$k_{to,2}$ = ethylene desorption rate constant, m^6/s kg
$k_{SBI–LB}$ = LB–SBI interaction cross-flow coefficient, 1/s
k_{WGS} = rate constant for water–gas shift reaction, kmol/kg s bar
${}^k_iK_j$ = total mass transfer coefficient of species j between the compartments i and k, m/s
K_{WGS} = equilibrium constant for water–gas shift reaction
l = mixing length (Nikuradse), m
m = Parameter
M_j = molecular mass of species j, kg/kmol
n = local bubble number density, m^{-3} reactor
n_i = bubbles numbers of the compartment I, m^{-3} reactor
P = reactor pressure, Pa
P_j = partial pressure of species j, Pa
r = radial coordinate, m
R = ideal-gas constant
R_c = rayon of the reactor, m
R_j = formation rate of species j, kmol/kg s
Re = Reynolds number, Re = $\frac{dv_{slip}}{v_{ls}}$
T = temperature, K
T_i = temperature of compartment i, K
T_i^* = temperature at the interface of gas compartment i and the associated liquid, K
T_{wi} = wall temperature, K
U_g = superficial gas velocity, m/s
U_{LB} = volumetric flux of the large bubbles m/s
U_{SB} = volumetric flux of the small bubbles, m/s

v_b = relative velocity of bubbles, m/s
v_g = interstitial gas velocity, m/s
v_i = interstitial velocity of compartment i, m/s
v_l = interstitial liquid velocity, m/s
v_{ls} = interstitial slurry velocity, m/s
v_{slip} = gas-slurry slip velocity, m/s
$\overline{V}_j^{\infty}$ = partial molar volume at infinite dilution, m^3/kmol
Z = axial coordinate, m

Greek letters

δ = maximum bubbles diameter in the column center, m
Δ_i = Sauter diameter of bubbles in compartment i, m
$\Delta H_{\phi,j}$ = vaporization enthalpy of species j, kJ/kmol
ΔH_{FT} = Fischer Tropsch reaction enthalpy, $kJ/kmol_{CO}$
ΔH_{WGS} = Water–gas shift reaction enthalpy, $kJ/kmol_{CO}$
ε_g = local gas holdup, m^3/m^3reactor
$\varepsilon_{g,tot}$ = total gas holdup, m^3/m^3reactor
ε_i = volumetric fraction of compartment i, m^3/m^3reactor
γ_j = activity coefficient
$\phi_{j,v}$ = vapor-phase fugacity coefficient
λ = dimensionless radius corresponding to maximum negative slurry velocity
$\widetilde{\lambda}_i$ = turbulent conductivity of compartment i, kJ/m s K
υ^{turb} = turbulent kinematic viscosity, m^2/s
υ_{ls} = kinematic viscosity of slurry, m^2/s
μ_l = dynamic viscosity of liquid phase, Pa s
μ_{ls} = dynamic viscosity of slurry, Pa s
μ_{LB} = dynamic viscosity of large bubbles, Pa s
ρ_g = gas density, kg/m^3
ρ_g^* = gas density at atmospheric pressure, kg/m^3
ρ_l = liquid density, kg/m^3
ρ_{ls} = suspension density, kg/m^3
ρ_p = catalyst density, kg/m^3solid
τ_{ls}^{turb} = turbulent shear stress, kg/m s^2
τ_w = wall shear stress, kg/m s^2
ξ = dimensionless radial coordinate

Abbreviations

FT = Fischer Tropsch
L = liquid
LI = liquid in core region
LII = liquid in annulus region
LB = large bubbles
LSI = slurry in core region
LSII = slurry in annulus region
SI = solid in core region
SII = solid in annulus region
SBI = small bubbles in core region
SBII = small bubbles in annulus
WGS = water–gas shift

Literature Cited

1. Thomas S, Dawe RA. Review of ways to transport natural gas energy from countries which do not need the gas for domestic use. *Energy*. 2003;28:1461–1477.
2. Font Freide JJHM, Gamlin TD, Graham C, Hensman JR, Nay B, Sharp C. An adventure in catalysis: The story of BP Fischer-Tropsch catalyst from laboratory to full-scale demonstration in Alaska. *Top Catal*. 2003;26:3–12.
3. Kato Y, Nishiwaki T, Fukuda T, Tanaka S. The behaviour of suspended solid suspended particles and liquid in bubble columns. *J Chem Eng Jpn*. 1972;5:112–120.
4. Deckwer WD, Sermemen Y, Ralek M, Schmidt B. Modeling of Fischer-Tropsch Synthesis in the slurry phase. *Ind Eng Chem Process Des Dev*. 1982;21:231–241.
5. Mills PL, Turner JR, Ramachandran PA, Dudukovic MP. The Fischer-Tropsch synthesis in slurry bubble column reactors: Analysis of reactor performance using the axial dispersion model. *Topics in Chemical Engineering*, Vol. 8. New York: Gordon & Breach Science Publishers, 1996.
6. de Swart JWA. *Scale-Up of a Fischer-Tropsch Slurry Reactor*, PhD Thesis. University of Amsterdam, Amsterdam, The Netherlands, 1996.
7. Maretto C, Krishna R. Modelling of a bubble column slurry reactor for Fischer-Tropsch synthesis. *Catal Today*. 1999;52:279–289.
8. Rados N, Al-Dahhan MH, Dudukovic MP. Dynamic modeling of slurry bubble column reactors, *Ind Eng Chem Res*. 2005;44:6086–6094.
9. Ahon VR, Costa JrEF, Monteagudo JEP, Fontes CE, Biscaia EC Jr, Lage PLC. A comprehensive mathematical model for Fischer-Tropsch synthesis in well-mixed slurry reactors. *Chem Eng Sci* 2005;60:677–694.
10. Stern D, Bell AT, Heinemann H. A theoretical model for the performance of bubble-column reactors used for Fischer-Tropsch synthesis. *Chem Eng Sci*. 1985;40:1665–1677.
11. de Swart JWA, Krishna R. Simulation of the transient and steady state behavior of a bubble column slurry reactor for Fischer-Tropsch Synthesis. *Chem Eng Process*. 2002;41:35–47.
12. Schluter S, Steiff A, Weinspach PM. Modeling and simulation of bubble column reactors. *Chem Eng Process*. 1992;31:97–117.
13. Rados N, Al-Dahhan MH, Dudukovic MP. Modeling of the Fischer-Tropsch synthesis in slurry bubble column reactors. *Catal Today*. 2003;79-80:211–218.
14. van Baten JM, Krishna R. Eulerian Simulation Strategy for Scaling up a bubble column slurry reactor for Fischer-Tropsch synthesis. *Ind Eng Chem Res*. 2004;43:4483–4493.
15. Murray P, Fan LS. Axial solid distribution in slurry bubble columns. *Ind Eng Chem Res*. 1989;28:1697–1703.
16. Bukur DB. Models for Fischer-Tropsch reaction in slurry bubble column reactors. *Chem Eng Sci*. 1983;38,440–446.
17. Bukur DB, Kumar VR. Effect of catalyst dispersion on performance of slurry bubble column reactors. *Chem Eng Sci*. 1986;41:1435–1444.
18. Sriram K, Mann R. Dynamic gas disengagement: A new technique foe assessing the behaviour of bubble columns. *Chem Eng Sci*. 1977;32:571–580.
19. Varmeer DJ, Krishna R. Hydrodynamics and mass transfer in bubble columns operating in the churn-turbulent regime. *Ind Eng Chem Process Des Dev*. 1981;20:475–482.
20. van der Laan GP, Beenackers AACM, Krishna R. Multicomponent reaction engineering model for Fe-catalyzed Fischer-Tropsch synthesis in commercial scale slurry bubble column reactors. *Chem Eng Sci*. 1999;54:5013–5019.
21. Shah YT, Joseph S, Smith DN, Ruether JA. Two-bubble class model for churn-turbulent bubble-column reactor. *Ind Eng Chem Process Des Dev*. 1985;24:1096–1104.
22. Modak SY, Juvekar VA, Rane VC. Comparison of the single-bubble-class and modified two-bubble-class models of bubble column reactors. *Chem Eng Technol*. 1994;17:313–320.
23. Krishna R, Sie ST. Design and scale-up of the Fischer-Tropsch bubble column slurry reactor. *Fuel Process Technol*. 2000;64:73–105.
24. Kantak MV, Hesketh RP, Kelkar BG. Effect of gas and liquid properties on gas-phase dispersion in bubble columns. *Chem Eng J*. 1995;59:91–98.
25. Hartland S, Mecklenburgh JCA. Comparison of differential and stagewise counter current extraction with backmixing. *Chem Eng Sci*. 1966;21:1209–1229.
26. Chianese AA. A mathematical model for a bubble column reactor for the cumene oxidation. *Chem Eng Commun*. 1982;17:261–270.
27. Leib TM, Mills PL, Lerou JJ, Turner JR. Evaluation of neural networks for simulation of three-phase bubble column reactors. *Chem Eng Res Des*. 1995;73:690–700.
28. Prakash A. On the effect of syngas composition and water-gas-shift reaction rate on FT synthesis over iron based catalyst in a slurry reactor. *Chem Eng Commun*. 1993;128:143–151.
29. Levenspiel O. *Chemical Reaction Engineering*, 2nd ed. New York: Wiley, 1972.
30. Chen P, Gupta P, Dudukovic MP, Toseland BA. Hydrodynamics of slurry bubble column during dimethyl ether (DME) synthesis: Gas-liquid recirculation model and radioactive tracer studies. *Chem Eng Sci*. 2006;61:6553–6570.
31. Jakobsen HA, Lindborg H, Dorao CA. Modeling of bubble column reactors: Progress and limitations. *Ind Eng Chem Res*. 2005;44:5107–5151.

32. Larachi F, Desvigne D, Donnat L, Schweich D. Simulating the effects of liquid circulation in bubble columns with internals. *Chem Eng Sci*. 2006;61:4195–4206.
33. Gupta P, Ong B, Al-Dahhan MH, Dudukovic MP, Toseland BA. Hydrodynamics of churn turbulent bubble columns: gas-liquid recirculation and mechanistic modeling. *Catal Today*. 2001;64:253–269.
34. Krishna R. A scale-up strategy for a commercial scale bubble column slurry reactor for Fischer-Tropsch synthesis. *Oil Gas Sci Technol*. 2000;55:359–372.
35. Sato Y, Sadatomi M, Sekoguchi K. Momentum and heat transfer in two-phase bubble flow. I. Theory. *Int J Multiphase Flow*. 1981;7:167–177.
36. Reichardt H. Vollstandige Darstellung der turbulenten Geschwindgkeitsverteilung in glatten Leitungen. *ZAMM*. 1951;31:208–215.
37. Riquarts HP. Flow profiles, change of momentum, and mixing of the liquid phase in bubble columns. *Chem Ing Tech*. 1981;53:60–61.
38. Zehner P. Momentum mass and heat transfer in bubble columns, Part 1: Flow model of the bubble column and liquid velocities. *Int Chem Eng*. 1986;26:22–35.
39. Wu Y, Ong B, Al-Dahhan MH. Prediction of axial liquid velocity profile in bubble column. *Chem Eng Sci*. 2001;56:1127–1130.
40. Rados N. *Slurry Bubble Column Hydrodynamics*, PhD Thesis. Washington University, St. Louis, 2003.
41. Forret A, Schweitzer JM, Gauthier R, Krishna R, Schweich D. Liquid dispersion in large bubble diameter columns, with and without internals. *Can J Chem Eng*. 2003;81:360–366.
42. Chen J, Li F, Degaleesan S, Gupta P, Al-Dahhan MH, Dudukovic MP, Toseland BA. Fluid dynamic parameters in bubble columns with internals. *Chem Eng Sci*. 1999;54:2187–2197.
43. Alper E, Wichtendahl B, Deckwer WD. Gas absorption mechanism in catalytic slurry reactors. *Chem Eng Sci*. 1980;35:217–222.
44. Taylor R, Krishna R. *Multicomponent Mass Transfer*. New York: Wiley, 1993.
45. Caldwell L, van Vuuren DS. On the formation and composition of the liquid phase in Fischer-Tropsch reactors. *Chem Eng Sci*. 1986;41:89–96.
46. Marano JJ. *Property Correlation and Characterization of Fischer-Tropsch Liquids from Process Modeling*, PhD Thesis. University of Pittsburgh, Pittsburgh, PA 1996.
47. Marano JJ, Holder GD. Characterization of Fischer-Tropsch liquids for vapor-liquid equilibria calculations. *Fluid Phase Equilib*. 1997;138:1–21.
48. Sanchez IC, Lacombe RH. Statistical thermodynamics of polymer solutions. *Macromolecules*. 1978;11:1145–1150.
49. Reid RC, Prausnitz JM, Poling BE. *The Properties of Gases and Liquids*, 4th ed. New York: McGraw Hill, 1987.
50. Deckwer WD, Louisi Y, Zaidi A, Ralek M. Hydrodynamic properties of the Fischer-Tropsch slurry process. *Ind Eng Chem Process Des Dev*. 1980;19,699–708.
51. Sanger P, Deckwer WD. Liquid-solid mass transfer in aerated suspensions. *Chem Eng J*. 1981;22:179–187.
52. Anderson RB. Catalysts for the Fischer-Tropsch synthesis. In: Emmett PH, editor. *Catalysis*. New York: Van Nostrand-Reinhold, 1956.
53. Yang CH, Massoth FE, Oblad AG. Kinetics of carbon monoxide and hydrogen reaction over cobalt-copper-aluminium oxide catalysts. *Adv Chem Ser*. 1979;178:35–45.
54. Sarup B, Wojciechowski BW. Studies of the Fischer-Tropsch synthesis on a cobalt catalyst. II. Kinetics of carbon monoxide conversion to methane and to higher hydrocarbons. *Can J Chem Eng*. 1989;67:62–69.
55. Yates IC, Satterfield CN. Intrinsic kinetics of the Fischer-Tropsch synthesis on a cobalt catalyst. *Energy Fuels*. 1991;5:168–1973.
56. Iglesia E, Reyes SC, Madon RJ, Soled SI. Selectivity control and catalyst design in Fischer-Tropsch synthesis: sites, pellets and reactors. *Adv Catal Relat Subj*. 1993;39:221–228.
57. Chanenchuk CA, Yates IC, Satterfield CN. The Fischer-Tropsch synthesis with mechanical mixture of a cobalt catalyst and a copper-based water-gas shift catalyst. *Energy Fuels*. 1991;5:847–855.
58. Anfray J. *Acquisition de données pour la modélisation d'une colonne a bulles Fischer-Tropsch*, PhD Thesis. Université Claude Bernard, Lyon, France, 2005.
59. Bremaud M, Fongarland P, Anfray J, Jallais S, Schweich D, Khodakov AY. Influence of syngas composition on the transient behavior of a Fischer–Tropsch continuous slurry reactor. *Catal Today*. 2005;106:137–142.
60. Anfray J, Brémaud M, Khodakov A, Jallais S, Schweich D. Kinetic study and modeling of Fischer-Tropsch reaction over a Co/Al_2O_3 catalyst in a slurry reactor. *Chem Eng Sci*. In press.
61. Keyser MJ, Everson RC, Espinoza RL. Fischer-Tropsch kinetic studies with cobalt-manganese oxide catalysts. *Ind Eng Chem Res*. 2000;39:48–54.
62. O'Dowd W, Smith DN, Ruther JA, Saxena SC. Gas and solids behavior in a baffled and unbaffled slurry bubble column. *AIChE J*. 1987;33:1958–1969.
63. Gandhi B, Prakash A. Bergougnou M.A. Hydrodynamic behavior of slurry bubble column at high solids concentration. *Powder Technol*. 1999;80:103–110.
64. Kato Y., Nishiwaki, A., Fukuda T., Tanaka S. The behavior of suspended solid particles and liquid in bubble columns. *J Chem Eng Jpn*. 1971;14:20–28.
65. Sokolichin A, Eigenberger G, Lapin A. Simulation of buoyancy driven bubbly flow: Established simplifications and open questions. *AIChE J*. 2004;50:24–45.

Appendix A: Lumping–Delumping Equations

The mass specific rate for the production of lump j (used into the species and enthalpy balance equations), $R^{\mathrm{r}}_{\lambda'-1+j}$ is a molar-mass weighted function of the $K+1$ species reaction rates $R^{\mathrm{s}}_{\mathrm{C}_{(K+1)(j-1)+k+\lambda'}\mathrm{H}_{2(K+1)(j-1)+2k+2\lambda'}}$ or $R^{\mathrm{s}}_{\mathrm{C}_{(K+1)(j-1)+k+\lambda'}\mathrm{H}_{2(K+1)(j-1)+2k+2\lambda'+2}}$:

$$R^{\mathrm{r},0}_{\lambda'+j-1}=\frac{\sum_{\mathrm{k}=0}^{\mathrm{K}} R^{\mathrm{s},0}_{\mathrm{C}_{(K+1)(j-1)+k+\lambda'}\mathrm{H}_{2(K+1)(j-1)+2k+2\lambda'}} M^{0}_{(K+1)(j-1)+k+\lambda'}}{\frac{1}{K+1}\sum_{\mathrm{k}=0}^{\mathrm{K}} M^{0}_{(K+1)(j-1)+k+\lambda'}} \quad \text{for } \alpha\text{-olefins} \tag{A1}$$

$$R^{\mathrm{r,p}}_{\lambda'+j-1}=\frac{\sum_{\mathrm{k}=0}^{\mathrm{K}} R^{\mathrm{s,p}}_{\mathrm{C}_{(K+1)(j-1)+k+\lambda'}\mathrm{H}_{2(K+1)(j-1)+2k+2\lambda'+2}} M^{\mathrm{p}}_{(K+1)(j-1)+k+\lambda'}}{\frac{1}{K+1}\sum_{\mathrm{k}=0}^{\mathrm{K}} M^{\mathrm{p}}_{(K+1)(j-1)+k+\lambda'}} \quad \text{for } n\text{-paraffins} \tag{A2}$$

For delumping, a backward route from pseudocomponent concentrations (obtained from the species mass balance) to the individual concentrations is needed for the calculation of the liquid phase composition for each species since these are needed in the species mass balance and the enthalpy balance equations. It was assumed that the mass of each pseudocomponent j is equally distributed over the $(K+1)$ components that belong to the pseudocomponent class.[9] Thus, the molar concentration of each component of the liquid phase is calculated by:

$$C_{(K+1)(j-1)+k+\lambda'}=\frac{1}{K+1}\frac{M_{\lambda'+j-1}}{M_{(K+1)(j-1)+k+\lambda'}}C_{\lambda'+j-1} \tag{A3}$$

where:

$$\frac{M_{\lambda'+j-1}}{M_{(K+1)(j-1)+k+\lambda'}}=\frac{(K+1)(j-1)+\frac{K}{2}+\lambda'+\frac{1}{7}}{(K+1)(j-1)+k+\lambda'+\frac{1}{7}} \quad \text{for } \alpha\text{-olefins} \tag{A4}$$

$$\frac{M_{\lambda'+j-1}}{M_{(K+1)(j-1)+k+\lambda'}} = \frac{(K+1)(j-1)+\frac{K}{2}+\lambda'}{(K+1)(j-1)+k+\lambda'} \quad \text{for } n\text{-paraffins} \tag{A5}$$

Appendix B: Fischer–Tropsch Intrinsic Kinetics

Fiscer–Tropsch CO and H_2 consumption rates (WGS reaction accounted for later)

$$-R_{CO} = R_{CH_4} + \sum_{i=2}^{n} i(R_{C_iH_{2i}} + R_{C_iH_{2i+2}}) \tag{B1}$$

$$-R_{H_2} = 3R_{CH_4} + \sum_{i=2}^{n} (2iR_{C_iH_{2i}} + (2i+1)R_{C_iH_{2i+2}}) \tag{B2}$$

Methane formation rate

$$R_{CH_4} = k_{tp,1}({}^*C_1)({}^*H) \tag{B3}$$

where,

$$({}^*C_1) = \frac{k_{{}^*C_1}({}^*H)({}^*CH_2)}{k_{tp_1}({}^*H) + k_p({}^*CH_2)} \tag{B4}$$

$$({}^*H) = \frac{C_t K_{H_2}^{1/2} C_{H_2}^{1/2}}{[1 + b_e C_{CO}^L]} \tag{B5}$$

$$({}^*CH_2) = \frac{-V + \sqrt{V^2 + 4U\frac{a_e C_{CO,L} C_{H_2,L}}{(1+b_e C_{CO,L})^2}}}{2U} \tag{B6}$$

$$U = \frac{k_p k_{{}^*C1}({}^*H)}{k_{tp}({}^*H) + k_{to}} \qquad V = k_{{}^*C1}({}^*H) + \frac{k_p k_a({}^*H)\sum_{j=2}^{\infty} C_{ol,j}^L}{k_{tp}({}^*H) + k_{to}} \tag{B7}$$

n-Paraffin formation rate ($n \geq 2$)

$$R_{C_nH_{2n+2}} = k_{tp}({}^*C_n)({}^*H) \tag{B8}$$

where:

$$({}^*C_n) = \alpha_A^{n-1}({}^*C_1) + \sum_{i=2}^{n} B_{n-i+2}\alpha_A^{i-2} C_{ol,n-i+2}^L \tag{B9}$$

$$\alpha_A = \frac{k_p({}^*CH_2)}{k_p({}^*CH_2) + k_{tp}({}^*H) + k_{to}}$$

$$B_n = \frac{k_a({}^*H)}{k_p({}^*CH_2) + k_{tp}({}^*H) + k_{to}}, \quad n > 2 \tag{B10}$$

Ethylene formation rate

$$R_{C_2H_4} = k_{t0,2}({}^*C_2) - k_{a,2} C_{ol,2}^L({}^*H) \tag{B11}$$

where:

$$({}^*C_2) = \alpha_{A,2}({}^*C_1) + B_2 C_{C_2H_4}^L \tag{B12}$$

$$\alpha_{A,2} = \frac{k_p({}^*CH_2)}{k_p({}^*CH_2) + k_{tp}({}^*H) + k_{to2}}$$

$$B_2 = \frac{k_{a2}({}^*H)}{k_p({}^*CH_2) + k_{tp}({}^*H) + k_{to2}} \tag{B13}$$

α-Olefins formation rate ($n \geq 3$)

$$R_{C_nH_{2n}} = k_{t0}({}^*C_n) - k_a C_{ol,n}^L({}^*H) \tag{B14}$$

Appendix C: Water Gas Shift Intrinsic Kinetics

$$R_{WGS} = k_{WGS} P^{0.75}\left(P_{CO} - \frac{P_{CO_2} P_{H_2}}{K_{WGS} P_{H_2O}}\right) \tag{C1}$$

where:

$$k_{WGS} = 8.0695\times 10^7 \exp\left[-\frac{149700}{RT}\right] \tag{C2}$$

$$K_{WGS} = \exp\left[-\frac{5078.0045}{T} - 5.8972089 + \frac{13.958681}{10^4}T - \frac{27.592844}{10^8}T^2\right] \tag{C3}$$

Manuscript received Mar. 6, 2007, and revision received May 14, 2007.